

Optical signatures of Euler superconductors

Chun Wang Chau,^{1,*} Wojciech J. Jankowski,¹ and Robert-Jan Slager^{2,1,†}

¹*TCM Group, Cavendish Laboratory, Department of Physics,
J J Thomson Avenue, Cambridge CB3 0HE, United Kingdom*

²*Department of Physics and Astronomy, University of Manchester,
Oxford Road, Manchester M13 9PL, United Kingdom*

(Dated: January 3, 2025)

We study optical manifestations of multigap band topology in multiband superconductors with a non-trivial topological Euler class. We introduce a set of lattice models for non-Abelian superconductors with the Euler invariant signified by a non-trivial quantum geometry. We then demonstrate that the topological Bogoliubov excitations realized in these models provide for a characteristic first-order optical response distinct from those of the other known topological superconductors. We find that the spectral distribution of the optical conductivity universally admits a topologically quantized jump and naturally differs from the features induced by the quantum geometry in the non-interacting bands without pairing terms. Further to uncovering observable signatures in first-order optical conductivities, we showcase that the higher-order nonlinear optical responses of the non-Abelian Euler superconductor can result in enhanced steady dc currents that fingerprint the exotic topological invariant. Finally, by employing a diagrammatic approach, we generalize our findings beyond the specific models of Euler superconductors.

I. INTRODUCTION

The study of topology in condensed matter systems, in particular topological insulators, semimetals, and superconductors, has been an active field for the last few decades [1–3]. While experimentally challenging [4–8], from a theoretical perspective, topological superconductors in particular host the intriguing possibility of being a platform for Majorana excitations [9–11]. Their interplay with topological insulators in engineered device setups, is of central interest, as these offer numerous promises to realize exotic proximity effects [10]. Last but not least, emergent Majorana zero modes are predicted to be usable for fault-tolerant topological quantum computation [12, 13].

Although single-gap topological insulators and topological semimetals are fairly extensively classified [14–21], recently novel multigap topological phases have been discovered [22]. In these systems, groups of bands, or band subspaces, carry previously uncharted multigap invariants [22–24]. A prominent example of a multigap invariant is the Euler class $\chi \in \mathbb{Z}$ [22, 25, 26], which characterizes systems described by real-valued Hamiltonians due to the presence of $\mathcal{C}_2\mathcal{T}$, i.e. two-fold rotation combined with time-reversal, or \mathcal{PT} , i.e. inversion combined with time-reversal symmetry. In such systems, the non-trivial Euler class can be associated with the non-Abelian band singularities. Mathematically, the band nodes are characterized by the same homotopy relations as the π -disclination defects in biaxial nematics [27–33]. Such band degeneracies carry non-Abelian quaternion frame charges, which can be manipulated by braiding nodes between multiple gaps in the momentum space [26, 31, 34].

As a result, momentum-space nodal braiding allows to have nodes with same charges within a two-band subspace. This ensures the Euler class attains a finite value, which pinpoints the pairs of nodes that can be merged, but cannot be annihilated. Their charges can otherwise be changed upon braiding with a band node in an adjacent band gap, which ensures a topological protection as long as the gap is maintained [26, 31, 32, 35].

Rather than remaining a purely theoretical pursuit, multigap invariants are increasingly retrieved in a wide range of systems. To date, they have been observed in trapped-ion experiments [36, 37], metamaterials [32, 38], and new directions include electron [31, 39, 40] and phonon band topologies [41, 42] of multiple materials simulated with first-principles calculations. Moreover, in the context of superconductors, we point out that recently the Euler class has also been predicted to induce an obstruction in the formation of Cooper pairs, which was suggested in the context of twisted graphene bilayers [43, 44]. A physical smoking-gun signature of the Euler class to experimentally validate these predictions in real materials remains therefore a central topic of interest. In this context, the previous studies considered optical manifestations, such as optical conductivities or higher-order bulk photovoltaic effects [45–47]. Similarly, transport signatures, including linear and non-linear anomalous Hall responses [48–50] were predicted to probe the topology of multigap topological insulators and semimetals [51]. In the case of topological superconductors included in the tenfold classification [15], the optical signatures were previously identified [52], while in the multigap case only the scattering signatures, such as Andreev reflections [53], have been discussed. In contrast, the optical responses of such exotic phases remain an open problem, which we address in this work. In this regard, the notions of quantum geometry [54–57], and their connections to the optical responses [57–59] are of

* cwc61@cam.ac.uk

† rjs269@cam.ac.uk

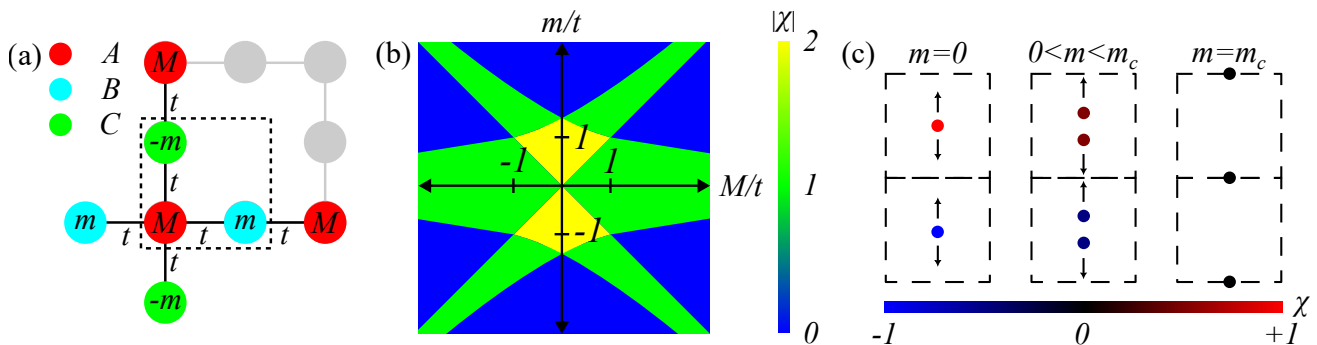


FIG. 1. Realizing non-trivial Euler class on the Lieb lattice. (a) Lattice structure of the tight-binding model. (b) Phase diagram realized in the model, as the onsite energy parameters M and m are changed. The phase is classified by the total patch Euler number of all nodes $\sum_n |\chi_n|$. (c) Example of splitting of the Euler node as we increase m . We split a single node of patch Euler class $\chi = 1$ located at Γ point, into two nodes of patch Euler class $\chi = 1/2$, which move in opposite directions towards Y point, or towards X point if we decrease m instead. For $m = m_c$, the nodes annihilate at the BZ edge on merging with their partners from the adjacent BZ, which results in a vanishing total Euler class $\chi = 0$.

particular interest for the superconducting states, given that quantum geometry naturally indicates the presence of non-trivial multigap invariants [45, 57], such as the Euler class. The importance and role of quantum geometry for the optical responses of superconducting states is most recently gaining an increasing recognition [60–65].

In this work, we investigate the optical response in superconductors realizing a non-trivial Euler class invariant, using concrete lattice models and a model-independent diagrammatic approach. We obtain signatures in the optical conductivity and higher-order photoconductivities, which are unique for superconducting systems, and that we further elucidate within the framework of quantum geometry. More specifically, starting from a tight binding model that hosts Euler bands on a Lieb lattice, we introduce intraband interactions, i.e. pairing terms, and construct a Bogoliubov-de-Gennes (BdG) Hamiltonian to describe a topological Euler superconductor at the mean-field level. We find that in the superconducting state tuning the phase difference between order parameters of the Euler bands can enhance optical transition between Euler nodes of different sectors, i.e. particle/hole (\pm) sectors, in the BdG Hamiltonian spectrum. Furthermore, we retrieve a quantized jump signature in the real part of the linear optical conductivity, which is proportional to the square of the Euler invariant and is induced by the singular quantum geometry realized in the Euler superconductor. We furthermore investigate noncentrosymmetric Euler superconductors, where both \mathcal{P} and \mathcal{T} symmetry are broken, which allows for non-vanishing responses at second order in optical fields. We then observe that the response is dominated by the injection currents, which are governed by the multiband quantum metric. However, we note that the intersector quantum metric, i.e. quantum metric combining states of both particle and hole sectors, exactly at the Euler node, is vanishing. Thus no direct topological, e.g. quantized, signature of the Euler class can be observed in the second-order response, unlike in the first-order response.

We further find that beyond the first-order optical response, there are topologically-enhanced diagrammatic contributions at third order in optical electric fields. In that context, we construct additional selection rules that arise from the difference in the coupling of electrons and holes with electromagnetic fields. We show that these could forbid certain third-order responses manifested in the normal state, but otherwise introduce new signatures that are unique to the superconducting system.

The paper is organized as follows. In Section II, we provide the details on realizations of Euler multiband superconductors adapted to lattice tight-binding models. In Sections III and IV, we correspondingly employ linear and nonlinear response theories to numerically benchmark the optical responses at linear and nonlinear orders. Section V then provides the diagrammatic analysis of the linear and nonlinear responses of non-Abelian Euler superconductors beyond the introduced specific models. In this context, we retrieve Euler class-induced topological contributions within one-loop diagrams for first- and third-order responses. We further discuss these findings in Section VI, before concluding and providing an outlook on the experimental feasibility of measuring the Euler superconductor invariant using optical probes, as applied to physical materials, in Section VII.

II. LIEB LATTICE MODEL

While most of our results are universal to general systems with a nodal Euler invariant, as we further elucidate within a diagrammatic approach, we start by considering a model on a Lieb lattice. The model is illustrated in Fig. 1(a) and the corresponding Hamiltonian reads

$$h_0(\mathbf{k}) = \begin{pmatrix} M & 2t \cos \frac{k_x}{2} & 2t \cos \frac{k_y}{2} \\ 2t \cos \frac{k_x}{2} & m & 0 \\ 2t \cos \frac{k_y}{2} & 0 & -m \end{pmatrix}. \quad (1)$$

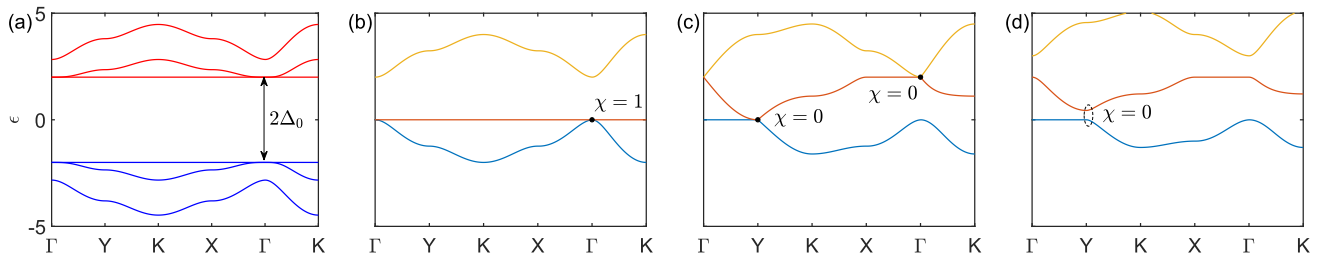


FIG. 2. Euler superconductor on the Lieb lattice. **(a)** Band structure for the BdG Euler Hamiltonian [Eq. (5)] with $t = 1$, $M = 2$, $m = 0$, and $\Delta_0 = 2$ for all bands. The electron sector (red) and hole sector (blue) are separated by a gap $2\Delta_0$. BdG band structures for particle sector generated from different phases in normal state. **(b)** Superconductor with a pair of Euler bands, with $M = 2t$, $m = 0$. **(c)** Doubly-nodal superconductor, where two trivial nodes are introduced in two neighboring gaps, with $M = m = t$. We note the doubly-nodal phase can also host nodes of non-vanishing patch Euler class. **(d)** Trivial superconducting phase, where all bands are gapped, with $M = 2t$, $m = t$.

The Hamiltonian in Eq. (1) satisfies the reality condition, as ensured by the \mathcal{PT} symmetry [31]. For convenience, we consider parameter pairs $(c_1, c_2) = (r \cos \theta, r \sin \theta) = (2t \cos \frac{k_x}{2}, 2t \cos \frac{k_y}{2})$, both with values ranging from $-2t$ to $2t$. On setting $m = 0$, the Hamiltonian $h_0(\mathbf{k})$ yields Bloch eigenvectors $u_i(\mathbf{k})$:

$$u_f = \begin{pmatrix} 0 \\ -\sin \theta \\ \cos \theta \end{pmatrix}, \quad (2)$$

$$u_{\pm} = \frac{1}{\sqrt{r^2 + \epsilon_{\pm}^2}} \begin{pmatrix} \epsilon_{-} \\ r \sin \theta \\ r \cos \theta \end{pmatrix}, \quad (3)$$

where $\epsilon_{\pm} = \frac{M}{2} \pm \sqrt{r^2 + \frac{M^2}{4}}$ represents the energy spectrum of the dispersive band. The model realizes a flat band located at energy $\epsilon_f = 0$, and has a quadratic band node between the flat band and dispersive band with energy ϵ_{-} (ϵ_{+}) for $M > 0$ ($M < 0$). The node realizes non-trivial band topology and quantum geometry associated with the Euler class invariant (see App. A). The Euler class χ_{ab} over a two-dimensional Brillouin zone (BZ) patch \mathcal{D} is defined as a topological obstruction to Stokes' theorem [26, 31]:

$$\chi_{ab}(\mathcal{D}) = \frac{1}{2\pi} \left[\int_{\mathcal{D}} [d\mathbf{k}] \text{Eu}_{ab}(\mathbf{k}) - \oint_{\partial\mathcal{D}} d\mathbf{k} \cdot \tilde{\xi}_{ab} \right], \quad (4)$$

which captures the singular non-Abelian multiband connection between bands a and b , $\tilde{\xi}_{ab}^{\mu} = \langle a | \partial^{\mu} b \rangle$, that determines the Euler curvature, $\text{Eu}_{ab} = \nabla_{\mathbf{k}} \times \tilde{\xi}_{ab}$; see App. A for more details. The invariant is non-vanishing and quantized ($\chi \in \mathbb{Z}$), if and only if the Hamiltonian is invariant under the action of $C_2\mathcal{T}$ or \mathcal{PT} symmetry. One can verify that the patch Euler class χ for the band node between the flat band and dispersive band amounts to $\chi = 1$.

A complete phase diagram of the model, as a function of M , m , is given in Fig. 1(b). We also illustrate the splitting of the Euler node of $\chi = 1$, into two nodes

which act as half-vortices in the multiband connection ($\chi = 1/2$) as we increase m from $m = 0$ in Fig. 1(c). For $M > 0$, we note that the split nodes evolve and annihilate at the BZ edge as we increase m to a critical value m_c , which results in a trivial phase via gap opening. Details of the band structure of different phases are illustrated in Fig. 2, where we present the bands for the Hamiltonian with non-trivial Euler class, for the multigap nodal phase, and for topologically trivial system realized in the model and in the descendent superconducting phase.

We now provide details on the superconducting phase supported by the introduced model in the presence of pairing interactions, as our main aim is to address the bulk physical signatures of the superconductor with non-trivial Euler class. At the mean-field level, we can describe the superconducting phase by introducing the Bogoliubov-de-Gennes (BdG) Hamiltonian:

$$H(\mathbf{k}) = \begin{pmatrix} h_0(\mathbf{k} - \mathbf{A}) & \Delta(\mathbf{k}) \\ \Delta^{\dagger}(\mathbf{k}) & -h_0(-\mathbf{k} - \mathbf{A})^T \end{pmatrix} \Big|_{\mathbf{A}=0}, \quad (5)$$

where we have assumed the order parameter does not couple to, or depend on, the vector gauge field \mathbf{A} . On restricting the superconductor pairing terms to intraband interactions (see App. B), the order parameter can be decomposed as:

$$\Delta(\mathbf{k}) = \sum_a \Delta_a |u_a(\mathbf{k})\rangle \langle u_a(\mathbf{k})|, \quad (6)$$

where $u_a(\mathbf{k})$ are the Bloch vectors of the normal state. The eigenstates $\tilde{u}_{a,s}$ of the BdG Hamiltonian thus can be related to the eigenstates of the normal state:

$$\tilde{u}_{a,s} = \frac{1}{\sqrt{1 + |\alpha_{a,s}|^2}} \begin{pmatrix} \alpha_{a,s} \\ 1 \end{pmatrix} \otimes u_a, \quad (7)$$

$$\alpha_{a,\pm} = \frac{\epsilon_a \pm \sqrt{|\Delta_a|^2 + \epsilon_a^2}}{\Delta_a^*}, \quad (8)$$

$$\tilde{\epsilon}_{a,\pm} = \pm \sqrt{\Delta_a^2 + \epsilon_a^2}, \quad (9)$$

where eigenstates of the BdG Hamiltonian $|\tilde{u}_{a,s}\rangle$ are indexed by a , i.e., the normal band index, and by $s = \pm 1$,

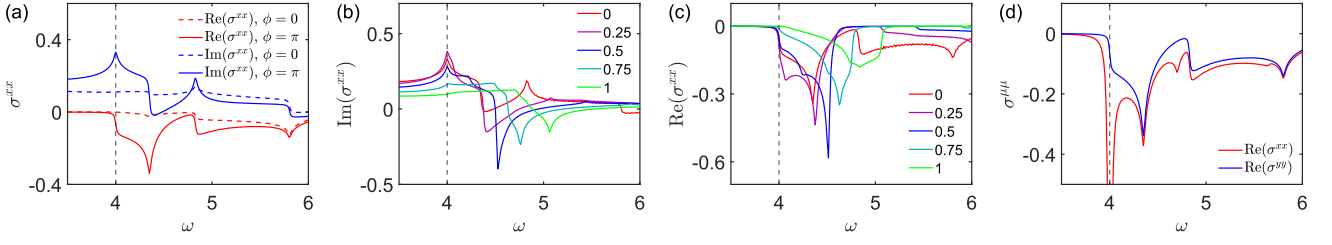


FIG. 3. First-order photoconductivity, with chemical potential exactly at the Euler node, and $M = 2$, $t = 1$, $\Delta_0 = 2$. We use vertical dashed line to denote the superconducting gap energy $2\Delta_0$ (a) Real part of conductivity (red), and imaginary part of σ^{xx} (blue), for $m = 0$. Notably, $\sigma^{xx} = \sigma^{yy}$ and $\sigma^{xy} = 0$ due to \mathcal{P} symmetry of the model. We further compare the cases with zero phase difference $\phi = 0$ in the order parameter (dashed line) and $\phi = \pi$ phase difference (solid line). When the phase difference is zero, the signature near the Euler node is suppressed. For the real part, there is a discrete jump of $e^2/(8\hbar)$ as a manifestation of the Euler class, as given by Eq. (27). (b) Imaginary part and (c) real part of σ^{xx} as we vary m . The Euler nodes are annihilated when $m = 0.73$, thus a discrete jump cannot be observed for $m = 0.75, 1$. (d) We introduce a \mathcal{P} -breaking term, along the x -direction. We note that the signature remains unchanged for σ^{yy} , as the y -direction respects the inversion symmetry, whereas the discrete jump evolves into a singular peak for σ^{xx} .

the sector index, with $+1$ (-1) corresponding to the electron (hole) sector. Having introduced the lattice model for an Euler superconductor, we now study the optical responses induced by the novel topological multiband invariant in the superconducting state.

III. LINEAR OPTICAL CONDUCTIVITY

We now address the linear optical conductivity in the introduced Euler superconductor. The linear optical conductivity captures ac current densities $j^\mu(\omega)$ in response to the optical electric field $E_\nu(\omega) = E_0 e^{i\omega t} + E_0^* e^{-i\omega t}$, with a frequency ω and field strength $|E_0|$, as:

$$j^\mu(\omega) = \sum_{\nu=x,y} \sigma^{\mu\nu}(\omega) E_\nu(\omega). \quad (10)$$

The optical conductivity derived within the linear response theory applied to the superconducting state [62] reads

$$\sigma^{\mu\nu}(\omega) = \frac{i}{2(\omega + i\eta)} \sum_{a,b} \left(\frac{J_{ab}^\mu J_{ba}^\nu f_{ab}}{\omega + i\eta - E_{ba}} + J_{ab}^{\mu\nu} f_a \delta_{ab} \right), \quad (11)$$

where $E_{ba} = \tilde{\epsilon}_{b,+} - \tilde{\epsilon}_{a,-}$, and $f_{ab} = f_a - f_b$ are the differences in the filling factors. Here we also set $\eta \rightarrow 0^+$, and defined the generalized velocity operator for a superconductor (see App. C) with a vector potential denoted as \mathbf{A} ,

$$J^{\mu_1 \dots \mu_n}(\mathbf{k}) = (-1)^n \frac{\partial H(\mathbf{k}, \mathbf{A})}{\partial A_{\mu_1} \dots \partial A_{\mu_n}} \Big|_{\mathbf{A} \rightarrow 0}. \quad (12)$$

We note that the generalized velocity operators can be naturally computed as numerical derivatives. As such, one can easily determine the linear optical conductivity, using Eq. (11), for a specific model, see App. D. In our case, using the above Lieb lattice model, we can investigate possible optical signatures that encapsulate the

Euler class. We do however note a minor but intricate complication when connecting the generalized velocity operator in quasiparticle band basis back to the velocity operator in normal state. Namely, because of the difference in coupling of the electron and hole sectors with the vector potential, the optical response associated with the topology of the Euler class originally present in the normal state is not necessarily inherited in the superconducting state. In Fig. 3, we report a numerical computation of the linear conductivity, where we fixed $M = 2$, $t = 1$, $\Delta_0 = 2$. To begin with, we note a difference in response, as we change the phase difference (ϕ) between the order parameter of the Euler bands (see App. B), as illustrated in Fig. 3(a). We moreover notice the suppression of response for $\phi = 0$. Meanwhile for $\phi = \pi$, at $\omega = 2\Delta_0$, which corresponds to the superconducting gap, we note a discrete jump for the real part, and a cusp-like profile for the imaginary part.

We further address whether the signature is intrinsically due to the Euler class, by varying m , which increased beyond the critical value $m_c \sim 0.73$ in our model parametrization, removes the Euler node. In Fig. 3(b), we observe that in the imaginary part of the conductivity, the cusp-like profile flattens as we gap out the Euler node, and the transition point is indistinct. In contrast, for the real part illustrated in Fig. 3(c), we note that a discrete conductivity jump persists, which remains relatively the same as we change m , as long as the patch Euler class is non-vanishing ($\chi \neq 0$). When the Euler node is gapped out, the discrete conductivity jump is no longer observable, showing a clear sign of transition, contrary to the imaginary part. For completeness, we also consider the case where inversion symmetry \mathcal{P} is broken along the x -direction, while keeping the \mathcal{PT} symmetry intact. We note that upon breaking the \mathcal{P} symmetry along the y -direction, the conductivity profile remains unchanged. However, for the x -direction, the discrete jump, previously observed at $\omega = 2\Delta_0$, evolves into a divergence, as the parity-odd velocity operator is now non-vanishing.

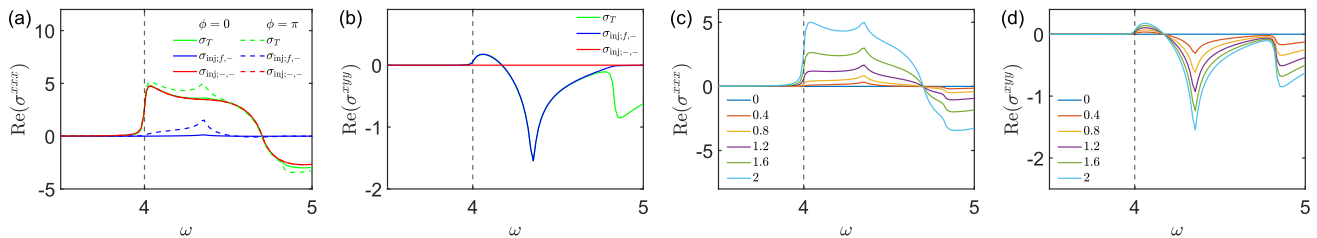


FIG. 4. Second-order photoconductivities in a noncentrosymmetric Euler superconductor. **(a)** Real part of σ^{xxxx} , when $M = 2$, $t = 1$, $t_2 = 2$, $\Delta_0 = 2$, $\eta = 10^{-2}$, and the injection conductivity contributions from different bands, for phase differences $\phi = 0$ and $\phi = \pi$. For both phase differences, the main contribution arises from $\sigma_{\text{inj};-,-}$ that corresponds to the transition between two bands that originate from the same normal state band. While the injection conductivity is proportional to the quantum metric, $\sigma_{\text{inj};-,-}$, the information about the geometry of the normal state cannot be directly inferred, as discussed in App. E. **(b)** Real part of σ^{xyy} . We observe that $\sigma_{\text{inj};-,-}$ vanishes, as the y -direction respects parity. Real part of **(c)** σ^{xxx} and **(d)** σ^{xyy} , for different values of t_2 . We note that the conductivities increase as we the parity breaking parameter t_2 is increased, with no major change to the spectral profile of the photoconductivities.

IV. HIGHER-ORDER RESPONSES

To address the higher-order responses of an Euler superconductor, we first study the second-order photoconductivities. The second-order photoconductivity $\sigma^{\mu\nu\rho}(\omega; \omega_1, \omega_2)$ obtains current densities,

$$j^\mu(\omega) = \sum_{\nu, \rho=x,y} \sigma^{\mu\nu\rho}(\omega; \omega_1, \omega_2) E_\nu(\omega_1) E_\rho(\omega_2), \quad (13)$$

as a function of the combined frequencies, $\omega = \omega_1 + \omega_2$, of a pair of optical fields $E_\nu(\omega_1), E_\rho(\omega_2)$. In the presence of \mathcal{P} -symmetry, even-order optical responses generically vanish. Thus, in a centrosymmetric system, the third-order response would be the next non-vanishing higher-order response. To obtain a non-vanishing second-order response, we can break \mathcal{P} -symmetry by adding parity-odd diagonal terms, which results in a modified Hamiltonian:

$$h_{\text{PB}}(\mathbf{k}) = h_0(\mathbf{k}) + t_2 \sin k_x \mathbb{1}_3. \quad (14)$$

We note that the eigenstates of the modified and original Hamiltonians are identical, thus the Euler node topology and the phase diagram remain unaltered. The dispersion is globally shifted by $t_2 \sin k_x$, since $\mathbb{1}_3 = \sum_a P_a(\mathbf{k})$, with $P_a(\mathbf{k})$ representing a projector onto band i . We can then promote the parity-breaking perturbation to the BdG Hamiltonian with a modified form:

$$H_{\text{PB}}(\mathbf{k}) = H(\mathbf{k}) + t_2 \sin k_x \mathbb{1}_6. \quad (15)$$

As such, the eigenstates of the BdG Hamiltonian under parity breaking term similarly remain unaltered, while the band energy dispersions are globally shifted by $t_2 \sin k_x$, since $\mathbb{1}_6 = \sum_{a,s} P_{a,s}(\mathbf{k})$, with $P_{a,s}$ a projector onto a BdG band. We delegate a further symmetry analysis of the parity effects central to the context of the second-order responses to App. E.

For responses that are second-order in optical fields, it is particularly interesting to address the possible dc current $j^\nu(0)$ responses, that is, in the limit $\omega \rightarrow 0$. In

particular, these are captured by the photoconductivities $\sigma^{\mu\nu\rho}(0; \omega_1, -\omega_1)$. We note that amongst such photoconductivities, the main contribution in the model Euler superconductor is due to the injection currents [65], with conductivity proportional to the quantum metric:

$$\sigma_{\text{inj}}^{\mu\nu\rho} = \frac{\pi}{4\eta} \sum_{a \neq b} (J_{aa}^\mu - J_{bb}^\mu) g_{ba}^{\nu\rho} f_{ab} \delta(\omega - E_{ba}), \quad (16)$$

and with η being the photoexcitation relaxation rate. Here, the imaginary part of the photoconductivity remains vanishing, and the multiband metric can be related to the generalized velocity operators via current operators $g_{ab}^{\nu\rho} = \Re \mathfrak{e} [J_{ab}^\nu J_{ba}^\rho / E_{ab}^2]$.

However, within the possible injection current responses, we observe no robust signature of the Euler class, as the intersector multiband metric between Euler bands is vanishing exactly at the node, see App. F. We note that the intersector injection current with $\omega \sim 2\Delta_0$ can be separated into two contributions, $\sigma_{\text{inj};f,-}$ and $\sigma_{\text{inj};-,-}$, which respectively correspond to metric $g_{f,+;-,-} = g_{f,-;-,+}$ and $g_{-,-;-,+} = g_{-,+;-,-}$. Fundamentally, the latter bears no information about the geometry of the normal state. Instead, it can be related purely to the characteristic band dispersion, rather than to the Euler band geometry or topology.

We demonstrate numerical results for the second-order photoconductivities in Fig. 4. For σ^{xxx} , we compare the case of $\phi = 0$ and $\phi = \pi$ phase differences in Fig. 4(a). In particular, for σ^{xxx} , the major contribution is $\sigma_{\text{inj};-,-}$, thus changing ϕ only affects the contribution that captures the multiband topology, and does not cause any significant change in the profile around $\omega = 2\Delta_0 = 4$. We do notice that the contribution from $\sigma_{\text{inj};f,-}$ is vanishing when $\phi = 0$, since the contribution captures the Euler class. For σ^{xyy} , as illustrated in Fig. 4(b), we note that $\sigma_{\text{inj};-,-}$ is now vanishing, since parity is not broken along the y -direction. Thus, the major contribution is $\sigma_{\text{inj};f,-}$. However, since the corresponding metric vanishes exactly at the node, no direct signature of the Euler class can be extracted. In Fig. 4(c-d) we change t_2 ,

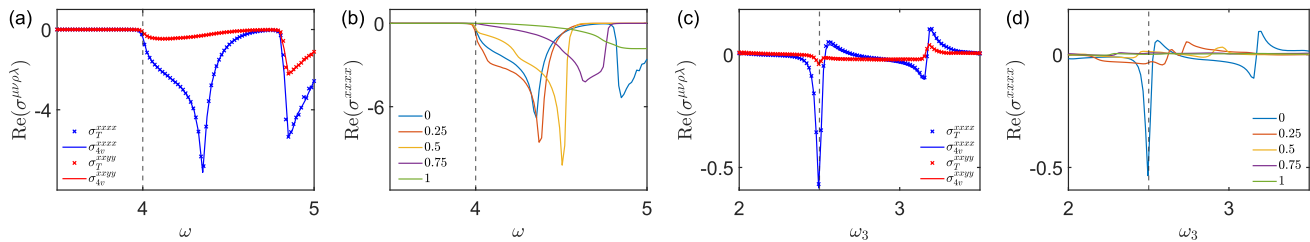


FIG. 5. Third-order photoconductivities in the Euler superconductor, with $M = 2$, $m = 0$, $t = 1$, $\Delta_0 = 2$, $\eta = 10^{-2}$. **(a)** Real part of the total conductivity $\sigma^{\mu\nu\rho\lambda}(\omega; -\omega, \omega, -\omega)$, and four-vertex contributions corresponding to the diagram Fig. 6(b), for σ^{xxxx} and σ^{xyyy} . We note that the four-vertex contribution is the major contribution. We also observe an increase $\propto \sqrt{\omega - 2\Delta_0}$ for σ^{xxxx} for $\omega > 2\Delta_0$. **(b)** Similarly to the linear conductivity, the increase persists, provided the Euler node is intact, as we illustrate by varying m . **(c)** We further present $\sigma^{\mu\nu\rho\lambda}(\omega; \omega_1, \omega_2, \omega_3)$, with $\omega_2 + \omega_3 = 2\Delta_0$ and $\omega_2 = 1.5$. Here, ω_1 matches the energy difference between the Euler node and the lowest BdG band. The dominant contribution also arises from the four-vertex diagram. **(d)** The optical signature gradually dissolves before the Euler node is annihilated, as m is varied in the model.

which corresponds to the relative strength of the parity-breaking term. We note that both $J_{aa}^\mu - J_{bb}^\mu$ and $g_{-,-,+}^{xx}$ increase linearly with t_2 , thus the conductivity increases roughly quadratically for σ^{xxx} and linearly for σ^{xyy} .

Furthermore, having studied the second-order responses of the noncentrosymmetric Euler superconductors, we can compute more general third-order responses to the optical fields. The associated current densities read

$$j^\mu(\omega) = \sum_{\nu, \rho, \lambda=x,y} \sigma^{\mu\nu\rho\lambda}(\omega; \omega_1, \omega_2, \omega_3) E_\nu(\omega_1) E_\rho(\omega_2) E_\lambda(\omega_3), \quad (17)$$

with third-order photoconductivity tensor elements $\sigma^{\mu\nu\rho\lambda}(\omega; \omega_1, \omega_2, \omega_3)$ and frequency $\omega = \omega_1 + \omega_2 + \omega_3$.

To fully understand the nature of the third-order photoconductivity analytically, we instead need a diagrammatic approach, which we discuss in the next section; see also App. G. We here first focus on discussing the numerical result, which we further verify within a diagrammatic approach in the next section. To begin, we investigate real part of the total conductivity $\sigma^{xxxx}(\omega; -\omega, \omega, -\omega)$ in Fig. 5(a), which corresponds to four virtual transitions combining the Euler bands between different sectors. We note that σ^{xyyy} is suppressed, compared to σ^{xxxx} . We also observe that the conductivity profile σ^{xxxx} is similar to σ^{xx} , with both enjoying a discrete jump at $\omega = 2\Delta_0$. To demonstrate the robustness of this correspondence, we thus change the value of m in Fig. 5(b), observing that the discrete jump remains intact, as long as the Euler node is not gapped out. Similarly to σ^{xx} , we note that the discrete jump is of universal magnitude, before the Euler nodes are annihilated as $m > 0.73$, when the jump can no longer be observed. However, as we will discuss, we note that the jump is not universally quantized, unlike in the linear case, as we further derive in App. H using the diagrammatic approach.

We are also interested in the case where $\omega_2 + \omega_3 = 2\Delta_0$, where we arbitrarily set $\omega_2 = 1.5$. To ensure that the calculated conductivity is mainly contributed by the Euler node, we set ω_1 , equal to the energy difference between the Euler node, and the lowest band, at the same mo-

mentum point. From Fig. 5(c), we note that σ^{xyyy} is similarly suppressed, when compared with σ^{xxxx} , and we note a peak when exactly $\omega_2 + \omega_3 = 2\Delta_0$, which we propose as a two-photon transition across the superconducting gap. We do note however, that as we change m in Fig. 5(d), the signature is significantly weakened even when the Euler node is not gapped out. To justify this effect, we remark that the additional bands hosting no Euler class also contribute to the third-order response.

V. DIAGRAMMATIC ANALYSIS

Previously, we used a response theory approach to calculate the optical conductivity for our specific model. However, such an approach proves difficult to provide clear general insights, linking the Euler class to the response observed numerically. In the following, we therefore analyze general diagrammatic features within linear and nonlinear response theories [66], which pinpoint the non-triviality of the Euler invariant in the superconducting state. We stress that these field-theoretic features are beyond the specific model realizations of the Euler superconductor, see App. G-K for full technical details. Given the numerically retrieved anomalous quantized jump in optical conductivity in Section III, we begin by analyzing the associated diagrammatics of the first-order optical conductivity.

The total first-order optical conductivity $\sigma^{\mu\nu}(\omega)$ of a superconductor can be decomposed in terms of two diagrammatic contributions, see Fig. 6(a,b) [65]. Accordingly, expressed in terms of Green's functions $G(k_0, \mathbf{k})$ corresponding to the propagators of quasiparticles with four-momenta $k^\mu = (k_0, \mathbf{k})$, the conductivity $\sigma^{\mu\nu}(\omega)$ is given by:

$$\sigma^{\mu\nu}(\omega) = \frac{i}{\omega} \int [d\mathbf{k}] \int dk_0 \text{Tr}[J^{\mu\nu}(\mathbf{k})G(k_0, \mathbf{k}) + J^\mu(\mathbf{k})G(k_0 + \omega, \mathbf{k})J^\nu(\mathbf{k})G(k_0, \mathbf{k})], \quad (18)$$

where $J^{\mu_1 \dots \mu_n}(\mathbf{k})$ is the n th order velocity operator in the superconducting state [62]. The velocity operator of

the superconducting state can be related to that of the normal state $j^{\mu_1 \dots \mu_n}(\mathbf{k})$, as long as the Hamiltonian is centrosymmetric, i.e. invariant under \mathcal{P} symmetry,

$$j^{\mu_1 \dots \mu_n}(\mathbf{k}) = \frac{\partial h(\mathbf{k})}{\partial k_{\mu_1} \dots \partial k_{\mu_n}} \quad (19)$$

$$\begin{aligned} J^{\mu_1 \dots \mu_n}(\mathbf{k}) &= (-1)^n \frac{\partial H(\mathbf{k}, \mathbf{A})}{\partial A_{\mu_1} \dots \partial A_{\mu_n}} \Big|_{\mathbf{A} \rightarrow 0} \\ &= \tau_z^{n+1} \otimes j^{\mu_1 \dots \mu_n}(\mathbf{k}), \end{aligned} \quad (20)$$

where $\tau_z = \text{diag}(1, -1)$ is the Pauli matrix in Nambu basis. We note that $G^{-1}(k_0, \mathbf{k}) = k_0 - H(\mathbf{k})$, which also defines the Green's function of the BdG Hamiltonian, can be decomposed as a tensor product,

$$G(k_0, \mathbf{k}) = \sum_a G_a(k_0, \mathbf{k}) \otimes P_a(\mathbf{k}), \quad (21)$$

$$G_a(k_0, \mathbf{k}) = \frac{1}{\omega_0^2 - \tilde{\epsilon}_a^2} \begin{pmatrix} k_0 + \epsilon_a & \Delta_a \\ \Delta_a^* & k_0 - \epsilon_a \end{pmatrix}. \quad (22)$$

We can now compute the conductivity using Eq. (18), in terms of the velocity operator of the normal state

$$\sigma^{\mu\nu}(\omega) = \frac{a}{\omega} \sum_{a,b} \int [d\mathbf{k}] j_{aa}^{\mu\nu} \delta_{ab} I_1 + j_{ab}^{\mu} j_{ba}^{\nu} I_2, \quad (23)$$

$$I_1 = \int dk_0 \text{Tr}[\tau_z G_a(k_0)], \quad (24)$$

$$I_2 = \int dk_0 \text{Tr}[G_b(k_0 + \omega) G_a(k_0)], \quad (25)$$

where $j_{aa}^{\mu\nu} = \partial^\mu \partial^\nu \epsilon_a$ and $j_{ab}^{\mu} = \epsilon_{ab} \xi_{ab}^{\mu}$, with $\epsilon_{ab} = \epsilon_a - \epsilon_b$ and $\xi_{ab}^{\mu} = i\langle a | \partial^\mu b \rangle$. The calculation of the integral I_1, I_2 is included within App. I. We can identify the first diagram as the Drude contribution, which contains no information about the geometry. For the rest of the Section, we will calculate only the second diagram, which encodes the information about the quantum geometry of our system. In particular, we are interested in the intersector response, since the intrasector response cannot be efficiently distinguished from the Drude contribution numerically.

Before proceeding, we should recall some features of Euler nodes, see also App. A. Firstly, the multiband connection is purely imaginary, due to the reality of the Hamiltonian, resulting in a vanishing Berry curvature $\Omega_{ab}^{\mu\nu} = -2\mathcal{J}\mathbf{m}[\xi_{ab}^{\mu} \xi_{ba}^{\nu}]$. Furthermore, the connection between the pair of Euler bands is inversely proportional to r around the Euler node, where r is the momentum-space distance from the node. These features have a direct physical consequence, particularly with regard to the real part of the conductivity, as we will discuss later. To proceed with an analytical calculation, we further make the following assumptions: (i) $|\Delta_a| = \Delta_0$ for all bands, (ii) we work in zero temperature limit, (iii) $h(\mathbf{k})$ is real and invariant under the action of \mathcal{P} , \mathcal{T} , and \mathcal{PT} symmetries, (iv) one of the bands is flat (i.e. $\epsilon_a = 0$) and touches a dispersive band, as known to occur commonly

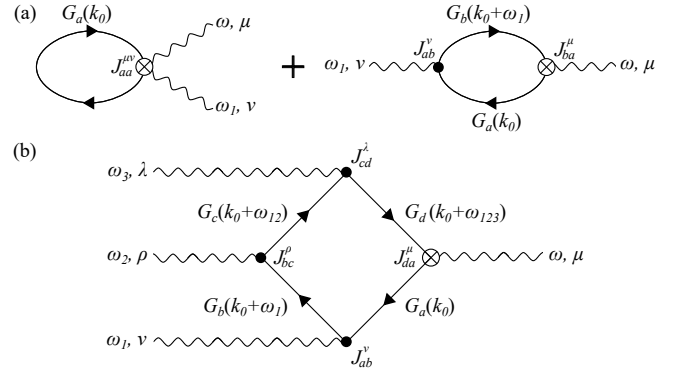


FIG. 6. One-loop diagrams corresponding to the topologically-induced anomalous optical responses of Euler superconductors. (a) First-order loop diagrams. (b) Third-order loop diagram capturing the enhanced third-order response of an Euler superconductor.

in Lieb and kagome lattices in the material context. At zero temperature, one retrieves only an intersector response, while due to \mathcal{P} -symmetry, σ^{xy} vanishes.

The total response between band indices a, b , namely $a, + \leftrightarrow b, -$ and $a, - \leftrightarrow b, +$, is:

$$\sigma^{\mu\mu}(\omega) = 2 \frac{i}{\omega} \int [d\mathbf{k}] \epsilon_j^2 |\xi_{ab}^{\mu}|^2 \frac{(\Delta_0 + \tilde{\epsilon}_b)(\Delta_0 \cos \phi - \tilde{\epsilon}_b)}{\tilde{\epsilon}_b[(\Delta_0 + \tilde{\epsilon}_b)^2 - \omega^2]}, \quad (26)$$

where ϕ is the phase difference between Δ_i and Δ_j . Despite the fact that the phase difference ϕ has no effect on the dispersion spectrum of the BdG Hamiltonian, we note that ϕ has a geometrical consequence, manifested in the multiband connection, by introducing a phase difference between Bloch band vectors. In particular, when $\omega = 2\Delta_0$, which corresponds to the transition between the nodes of electron and hole sectors, $\sigma^{\mu\mu} \propto 1 - \cos \phi$. Namely, the response is suppressed when $\phi = 0$, and maximized when $\phi = \pi$. The analytical finding quantitatively agrees with the numerical result in Fig. 3.

Due to the aforementioned $\xi_{ab}^{\mu} \propto r^{-1}$ dependency around the Euler node, for each Euler node of Euler class χ and dispersion $\epsilon_j \propto r^n$, such scalings introduce a quantized jump in $\Re[\sigma^{\mu\mu}]$, on crossing the gap energy $\omega = 2\Delta_0$:

$$\Re[\sigma^{\mu\mu}(\omega \rightarrow 2\Delta_0^+)] = \frac{e^2}{8\hbar} \frac{\chi^2}{n} (1 - \cos \phi). \quad (27)$$

This precisely corresponds to the optical conductivity jump of $e^2/(8\hbar)$ in the Lieb lattice, as the singular node with Euler class $\chi = 1$ is quadratic, when $m = 0$. In particular, when the Euler node is split for $m \neq 0$, each resulting node carries a patch Euler class of $\chi = 1/2$, and is approximately linear in dispersion. This splitting results in a discrete jump in optical conductivity, which is close to $e^2/(8\hbar)$. To demonstrate that these features are universal, we also retrieve an analogous discrete conductivity jump due to an Euler node in a kagome lattice model, as detailed and illustrated in App. L.

On the contrary, for second-order conductivity, the results can be well understood within the nonlinear response theory, where the injection current is the major contribution, and no topological terms are acquired. Thus, we leave the discussion of the diagrammatics for the second-order response out of this work.

At third order in optical fields, we find that the dominant contribution arises from a loop diagram introducing four quasiparticle propagators that target the pairs of Euler bands twice, see Fig. 6(b). This observation has been verified numerically in Fig. 5(a, c). We note that the analytical calculation is mostly analogous to the linear case and is therefore detailed in App. H. From the diagrammatic approach, one can deduce that the individual contributions per momentum space point \mathbf{k} scale with the square of the Euler curvature. We also note that differently from linear conductivity, where we retrieved a quantized jump from the Euler class, the increase of third-order photoconductivity observed in Fig. 5(a) is continuous, and $\sigma^{xxxx} \propto \sqrt{\omega - 2\Delta_0}$; see also App. H. Finally, contrary to the normal state [45], we note that all diagrams corresponding to the jerk conductivities [67] contributed by the transitions only between Euler bands in the particle and hole sectors are suppressed due to a set of third-order selection rules. The third-order selection rules are derived and further detailed in App. J.

VI. DISCUSSION

We further comment on the nature and applicability of our findings concerning the optical responses of Euler superconductors. First, it should be noted that anomalous optical conductivity was previously reported in multiorbital superconductors in Ref. [61]. Here, we show that a certain class of multiorbital, i.e. multiband, superconductors with non-trivial Euler class moreover inherits a *quantization* in the anomalous quantum-geometric first-order photoconductivity response. We unravelled the topological and geometric character of this anomaly with the diagrammatic perspective in the previous Section. In that regard, we also note that within the applied assumptions of intraband interactions, i.e. pairings, the vertex correction remains purely of intraband character. Therefore, the intersector contributions to the linear response are not modified when we introduce vertex corrections, as we also demonstrate in App. K. The vertex corrections contributed by the anomalous propagators admitting hybridized interband pairing channels provide for an interesting future direction to investigate.

In contrast to the normal Euler phases, such as Euler semimetals, we find distinct effects at the third order in electric fields. Namely, the jerk photoconductivity ratios no longer take values inherited from the Euler class [45], as soon as the pairing terms are introduced. Instead, we identified a one-loop four-vertex third-order response diagram that provides a topological enhancement rather than a quantization, which can be further

traced to the quantum geometry associated with the Euler invariant [57, 68].

While both the first- and third-order optical features are generic to the Euler invariant, given the diagrammatic and geometric nature of these anomalies, the second-order responses remain model-dependent. We showed that the strength of an inversion symmetry-breaking perturbation can significantly alter the response of an Euler superconductor and the injection currents cannot be diagrammatically associated with the non-trivial Euler class.

Our findings shed a light on the experimentally measurable optical responses in Lieb or kagome superconductors, which in particular correspond to the lattices that naturally realize the Euler class invariant. Importantly, a class of cuprate superconductors can be modelled with Lieb lattice Hamiltonians [69], which offers for further interesting connections of our analysis to the exotic correlated states experimentally realizable in these systems. The phase sensitive character of the optical responses further allows to optically distinguish Euler superconductors from the other known topological superconductors. Finally, the interplay of the superconducting Euler invariant, quantum geometry, and different possible multiband pairings in the presence of additional bands or disorder, remains an attractive direction for future studies.

VII. CONCLUSION AND OUTLOOK

We studied anomalous optical signatures of superconductors with a non-trivial multiband Euler class invariant. We introduced a tunable Lieb lattice model for an Euler superconductor. We found that the superconducting Euler invariant introduces anomalous quantized first-order and enhanced third-order optical responses. We further recast these signatures in terms of diagrammatics at the one-loop order that are applicable to general topological superconductors. We expect our findings to be relevant to the superconducting states realized on Lieb and kagome lattices, where the non-trivial Euler class can be naturally induced. Our results show that the presence of an exotic multigap topological invariant can be unravelled with anomalous optical responses in multiband superconductors.

ACKNOWLEDGMENTS

The authors thank Arthur S. Morris for discussions about non-Abelian topologies and superconductivity. C.W.C. acknowledges funding from the Croucher Cambridge International Scholarship by the Croucher Foundation and the Cambridge Trust. W.J.J. acknowledges funding from the Rod Smallwood Studentship at Trinity College, Cambridge. R.-J.S. acknowledges funding from a New Investigator Award, EPSRC Grant No. EP/W00187X/1, a EPSRC ERC underwrite Grant No.

-
- [1] X.-L. Qi and S.-C. Zhang, Topological insulators and superconductors, *Reviews of Modern Physics* **83**, 1057 (2011), [arXiv:1008.2026 \[cond-mat.mes-hall\]](#).
- [2] M. Z. Hasan and C. L. Kane, Colloquium: Topological insulators, *Reviews of Modern Physics* **82**, 3045 (2010), [arXiv:1002.3895 \[cond-mat.mes-hall\]](#).
- [3] N. P. Armitage, E. J. Mele, and A. Vishwanath, Weyl and Dirac semimetals in three-dimensional solids, *Reviews of Modern Physics* **90**, 015001 (2018), [arXiv:1705.01111 \[cond-mat.str-el\]](#).
- [4] R. M. Lutchyn, J. D. Sau, and S. Das Sarma, Majorana fermions and a topological phase transition in semiconductor-superconductor heterostructures, *Phys. Rev. Lett.* **105**, 077001 (2010).
- [5] V. Mourik, K. Zuo, S. M. Frolov, S. R. Plissard, E. P. A. M. Bakkers, and L. P. Kouwenhoven, Signatures of Majorana fermions in hybrid superconductor-semiconductor nanowire devices, *Science* **336**, 1003–1007 (2012).
- [6] S. D. Sarma, M. Freedman, and C. Nayak, Majorana zero modes and topological quantum computation, *npj Quantum Information* **1**, [10.1038/npjqi.2015.1](#) (2015).
- [7] S. Zhu, L. Kong, L. Cao, H. Chen, M. Papaj, S. Du, Y. Xing, W. Liu, D. Wang, C. Shen, F. Yang, J. Schneeloch, R. Zhong, G. Gu, L. Fu, Y.-Y. Zhang, H. Ding, and H.-J. Gao, Nearly quantized conductance plateau of vortex zero mode in an iron-based superconductor, *Science* **367**, 189–192 (2020).
- [8] A. Yazdani, F. von Oppen, B. I. Halperin, and A. Yacoby, Hunting for Majoranas, *Science* **380**, [10.1126/science.ade0850](#) (2023).
- [9] A. Y. Kitaev, Unpaired Majorana fermions in quantum wires, *Physics-Uspekhi* **44**, 131 (2001).
- [10] L. Fu and C. L. Kane, Superconducting proximity effect and Majorana fermions at the surface of a topological insulator, *Phys. Rev. Lett.* **100**, 096407 (2008).
- [11] C. Beenakker, Search for Majorana fermions in superconductors, *Annual Review of Condensed Matter Physics* **4**, 113–136 (2013).
- [12] A. Kitaev, Anyons in an exactly solved model and beyond, *Annals of Physics* **321**, 2–111 (2006).
- [13] C. Nayak, S. H. Simon, A. Stern, M. Freedman, and S. Das Sarma, Non-Abelian anyons and topological quantum computation, *Rev. Mod. Phys.* **80**, 1083 (2008).
- [14] A. P. Schnyder, S. Ryu, A. Furusaki, and A. W. W. Ludwig, Classification of topological insulators and superconductors in three spatial dimensions, *Phys. Rev. B* **78**, 195125 (2008).
- [15] A. Kitaev, Periodic table for topological insulators and superconductors, *AIP Conference Proceedings* **1134**, 22 (2009), <https://aip.scitation.org/doi/pdf/10.1063/1.3149495>.
- [16] R.-J. Slager, A. Mesaros, V. Juričić, and J. Zaanen, The space group classification of topological band-insulators, *Nat. Phys.* **9**, 98 (2013).
- [17] K. Shiozaki and M. Sato, Topology of crystalline insulators and superconductors, *Phys. Rev. B* **90**, 165114 (2014).
- [18] J. Kruthoff, J. de Boer, J. van Wezel, C. L. Kane, and R.-J. Slager, Topological classification of crystalline insulators through band structure combinatorics, *Phys. Rev. X* **7**, 041069 (2017).
- [19] R.-J. Slager, The translational side of topological band insulators, *J. Phys. Chem. Solids* **128**, 24 (2019), spin-Orbit Coupled Materials.
- [20] H. C. Po, A. Vishwanath, and H. Watanabe, Symmetry-based indicators of band topology in the 230 space groups, *Nat. Commun.* **8**, 50 (2017).
- [21] B. Bradlyn, L. Elcoro, J. Cano, M. G. Vergniory, Z. Wang, C. Felser, M. I. Aroyo, and B. A. Bernevig, Topological quantum chemistry, *Nature* **547**, 298 (2017).
- [22] A. Bouhon, T. Bzdusek, and R.-J. Slager, Geometric approach to fragile topology beyond symmetry indicators, *Phys. Rev. B* **102**, 115135 (2020).
- [23] Z. Davoyan, W. J. Jankowski, A. Bouhon, and R.-J. Slager, Three-dimensional \mathcal{PT} -symmetric topological phases with a Pontryagin index, *Phys. Rev. B* **109**, 165125 (2024).
- [24] A. Bouhon, Y.-Q. Zhu, R.-J. Slager, and G. Palumbo, Second Euler number in four-dimensional matter, *Phys. Rev. B* **110**, 195144 (2024).
- [25] A. Bouhon, A. M. Black-Schaffer, and R.-J. Slager, Wilson loop approach to fragile topology of split elementary band representations and topological crystalline insulators with time-reversal symmetry, *Phys. Rev. B* **100**, 195135 (2019).
- [26] J. Ahn, S. Park, and B.-J. Yang, Failure of Nielsen-Ninomiya Theorem and Fragile Topology in Two-Dimensional Systems with Space-Time Inversion Symmetry: Application to Twisted Bilayer Graphene at Magic Angle, *Phys. Rev. X* **9**, 021013 (2019).
- [27] Q. Wu, A. A. Soluyanov, and T. Bzdušek, Non-Abelian band topology in noninteracting metals, *Science* **365**, 1273 (2019).
- [28] G. E. Volovik and V. P. Mineev, Investigation of singularities in superfluid He³ in liquid crystals by the homotopic topology methods, in *Basic Notions Of Condensed Matter Physics* (CRC Press, 2018) pp. 392–401.
- [29] K. Liu, J. Nissinen, R.-J. Slager, K. Wu, and J. Zaanen, Generalized Liquid Crystals: Giant Fluctuations and the Vestigial Chiral Order of *I*, *O*, and *T* Matter, *Phys. Rev. X* **6**, 041025 (2016).
- [30] A. J. Beekman, J. Nissinen, K. Wu, K. Liu, R.-J. Slager, Z. Nussinov, V. Cvetkovic, and J. Zaanen, Dual gauge field theory of quantum liquid crystals in two dimensions, *Phys. Rep.* **683**, 1 (2017), dual gauge field theory of quantum liquid crystals in two dimensions.
- [31] A. Bouhon, Q. Wu, R.-J. Slager, H. Weng, O. V. Yazyev, and T. Bzdušek, Non-Abelian reciprocal braiding of Weyl points and its manifestation in ZrTe, *Nature Physics* **16**, 1137 (2020).
- [32] B. Jiang, A. Bouhon, Z.-K. Lin, X. Zhou, B. Hou, F. Li, R.-J. Slager, and J.-H. Jiang, Experimental observation of non-Abelian topological acoustic semimetals and their phase transitions, *Nature Physics* **17**, 1239–1246 (2021).

- [33] G. P. Alexander, B. G.-g. Chen, E. A. Matsumoto, and R. D. Kamien, Colloquium: Disclination loops, point defects, and all that in nematic liquid crystals, *Rev. Mod. Phys.* **84**, 497 (2012).
- [34] A. Bouhon and R.-J. Slager, Multi-gap topological conversion of Euler class via band-node braiding: minimal models, *PT*-linked nodal rings, and chiral heirs (2022), [arXiv:2203.16741](https://arxiv.org/abs/2203.16741) [cond-mat.mes-hall].
- [35] W. J. Jankowski, M. Noormandipour, A. Bouhon, and R.-J. Slager, Disorder-induced topological quantum phase transitions in multigap Euler semimetals, *Physical Review B* **110**, [10.1103/physrevb.110.064202](https://doi.org/10.1103/physrevb.110.064202) (2024).
- [36] F. N. Ünal, A. Bouhon, and R.-J. Slager, Topological Euler class as a dynamical observable in optical lattices, *Phys. Rev. Lett.* **125**, 053601 (2020).
- [37] W. Zhao, Y.-B. Yang, Y. Jiang, Z. Mao, W. Guo, L. Qiu, G. Wang, L. Yao, L. He, Z. Zhou, Y. Xu, and L. Duan, Quantum simulation for topological Euler insulators, *Communications Physics* **5**, 223 (2022).
- [38] B. Jiang, A. Bouhon, S.-Q. Wu, Z.-L. Kong, Z.-K. Lin, R.-J. Slager, and J.-H. Jiang, Observation of an acoustic topological Euler insulator with meronic waves, *Science Bulletin* **69**, 1653 (2024).
- [39] S. H. Lee, Y. Qian, and B.-J. Yang, Euler band topology in spin-orbit coupled magnetic systems (2024), [arXiv:2404.16383](https://arxiv.org/abs/2404.16383) [cond-mat.mes-hall].
- [40] A. Bouhon, G. F. Lange, and R.-J. Slager, Topological correspondence between magnetic space group representations and subdimensions, *Phys. Rev. B* **103**, 245127 (2021).
- [41] B. Peng, A. Bouhon, B. Monserrat, and R.-J. Slager, Phonons as a platform for non-Abelian braiding and its manifestation in layered silicates, *Nature Communications* **13**, 423 (2022).
- [42] B. Peng, A. Bouhon, R.-J. Slager, and B. Monserrat, Multigap topology and non-Abelian braiding of phonons from first principles, *Phys. Rev. B* **105**, 085115 (2022).
- [43] J. Yu, Y.-A. Chen, and S. Das Sarma, Euler-obstructed cooper pairing: Nodal superconductivity and hinge Majorana zero modes, *Phys. Rev. B* **105**, 104515 (2022).
- [44] J. Yu, M. Xie, F. Wu, and S. Das Sarma, Euler-obstructed nematic nodal superconductivity in twisted bilayer graphene, *Phys. Rev. B* **107**, L201106 (2023).
- [45] W. J. Jankowski, A. S. Morris, A. Bouhon, F. N. Ünal, and R.-J. Slager, Optical manifestations of topological Euler class, [arXiv e-prints](https://arxiv.org/abs/2311.07545), [arXiv:2311.07545](https://arxiv.org/abs/2311.07545) (2023), [arXiv:2311.07545](https://arxiv.org/abs/2311.07545) [cond-mat.mes-hall].
- [46] W. J. Jankowski and R.-J. Slager, Quantized integrated shift effect in multigap topological phases, *Phys. Rev. Lett.* **133**, 186601 (2024).
- [47] W. J. Jankowski, A. S. Morris, Z. Davoyan, A. Bouhon, F. N. Ünal, and R.-J. Slager, Non-Abelian Hopf-Euler insulators, *Phys. Rev. B* **110**, 075135 (2024).
- [48] F. D. M. Haldane, Model for a quantum Hall effect without Landau levels: Condensed-matter realization of the "parity anomaly", *Phys. Rev. Lett.* **61**, 2015 (1988).
- [49] Y. Gao, S. A. Yang, and Q. Niu, Field induced positional shift of Bloch electrons and its dynamical implications, *Phys. Rev. Lett.* **112**, 166601 (2014).
- [50] Y. Gao, Z.-Q. Zhang, and K.-H. Ding, Third-order nonlinear Hall effect in two-dimensional Dirac systems, *New Journal of Physics* **25**, 053013 (2023).
- [51] A. Jain, W. J. Jankowski, and R.-J. Slager, Anomalous geometric transport signatures of topological Euler class (2024), [arXiv:2412.01810](https://arxiv.org/abs/2412.01810) [cond-mat.mes-hall].
- [52] J. J. He, Y. Tanaka, and N. Nagaosa, Optical responses of chiral Majorana edge states in two-dimensional topological superconductors, *Phys. Rev. Lett.* **126**, 237002 (2021).
- [53] A. S. Morris, A. Bouhon, and R.-J. Slager, Andreev reflection in Euler materials, *New Journal of Physics* **26**, 023014 (2024).
- [54] J. Provost and G. Vallee, Riemannian structure on manifolds of quantum states, *Communications in Mathematical Physics* **76**, 289 (1980).
- [55] S. Peotta and P. Törmä, Superfluidity in topologically nontrivial flat bands, *Nature Communications* **6**, [10.1038/ncomms9944](https://doi.org/10.1038/ncomms9944) (2015).
- [56] P. Törmä, Essay: Where can quantum geometry lead us?, *Phys. Rev. Lett.* **131**, 240001 (2023).
- [57] A. Bouhon, A. Timmel, and R.-J. Slager, Quantum geometry beyond projective single bands (2023), [arXiv:2303.02180](https://arxiv.org/abs/2303.02180) [cond-mat.mes-hall].
- [58] J. Ahn, G.-Y. Guo, and N. Nagaosa, Low-frequency divergence and quantum geometry of the bulk photovoltaic effect in topological semimetals, *Phys. Rev. X* **10**, 041041 (2020).
- [59] J. Ahn, G.-Y. Guo, N. Nagaosa, and A. Vishwanath, Riemannian geometry of resonant optical responses, *Nature Physics* **18**, 290–295 (2021).
- [60] J. Ahn and N. Nagaosa, Theory of optical responses in clean multi-band superconductors, *Nature Communications* **12**, [10.1038/s41467-021-21905-x](https://doi.org/10.1038/s41467-021-21905-x) (2021).
- [61] W. Chen and W. Huang, Quantum-geometry-induced intrinsic optical anomaly in multiorbital superconductors, *Phys. Rev. Res.* **3**, L042018 (2021).
- [62] H. Watanabe, A. Daido, and Y. Yanase, Nonreciprocal optical response in parity-breaking superconductors, *Phys. Rev. B* **105**, 024308 (2022), [arXiv:2109.14866](https://arxiv.org/abs/2109.14866) [cond-mat.supr-con].
- [63] H. Tanaka, H. Watanabe, and Y. Yanase, Nonlinear optical responses in noncentrosymmetric superconductors, *Physical Review B* **107**, [10.1103/physrevb.107.024513](https://doi.org/10.1103/physrevb.107.024513) (2023).
- [64] H. Tanaka, H. Watanabe, and Y. Yanase, Nonlinear optical responses in superconductors under magnetic fields: quantum geometry and topological superconductivity (2024), [arXiv:2403.00494](https://arxiv.org/abs/2403.00494) [cond-mat.supr-con].
- [65] S. Watanabe and H. Watanabe, A gauge-invariant formulation of optical responses in superconductors, [arXiv e-prints](https://arxiv.org/abs/2410.18679), [arXiv:2410.18679](https://arxiv.org/abs/2410.18679) (2024), [arXiv:2410.18679](https://arxiv.org/abs/2410.18679) [cond-mat.supr-con].
- [66] D. E. Parker, T. Morimoto, J. Orenstein, and J. E. Moore, Diagrammatic approach to nonlinear optical response with application to Weyl semimetals, *Phys. Rev. B* **99**, 045121 (2019), [arXiv:1807.09285](https://arxiv.org/abs/1807.09285) [cond-mat.str-el].
- [67] B. M. Fregoso, R. A. Muniz, and J. E. Sipe, Jerk current: A novel bulk photovoltaic effect, *Phys. Rev. Lett.* **121**, 176604 (2018).
- [68] F. Xie, Z. Song, B. Lian, and B. A. Bernevig, Topology-bounded superfluid weight in twisted bilayer graphene, *Phys. Rev. Lett.* **124**, 167002 (2020).
- [69] K. Yamazaki, M. Ochi, D. Ogura, K. Kuroki, H. Eisaki, S. Uchida, and H. Aoki, Superconducting mechanism for the cuprate $\text{Ba}_2\text{CuO}_{3+\delta}$ based on a multiorbital Lieb lattice model, *Phys. Rev. Res.* **2**, 033356 (2020).

Appendix A: Euler class and quantum geometry

In this Section, we provide further details on the Euler class as well as on the quantum geometry induced by this multigap topological invariant.

The Euler class is defined with the non-Abelian Euler connection between band a and b [26, 31]:

$$\tilde{\xi}_{ab}^\mu = \langle a | \partial^\mu b \rangle, \quad (\text{A1})$$

with which we can define the Euler form $\text{Eu}_{ab} = d\tilde{\xi}_{ab}$ as an exterior derivative of the connection 1-form between band a and b ,

$$\text{Eu}_{ab} = \langle \partial^x a | \partial^y b \rangle - \langle \partial^y a | \partial^x b \rangle. \quad (\text{A2})$$

As mentioned in the main text, the Euler class χ_{ab} over a two-dimensional Brillouin zone (BZ) patch \mathcal{D} reads [26]:

$$\chi_{ab}(\mathcal{D}) = \frac{1}{2\pi} \left[\int_{\mathcal{D}} [d\mathbf{k}] \text{Eu}_{ab}(\mathbf{k}) - \oint_{\partial\mathcal{D}} d\mathbf{k} \cdot \xi_{ab} \right] \quad (\text{A3})$$

Centrally to this work, the presence of Euler invariant induces topologically-enhanced quantum geometry, which drives the optical response of an Euler superconductor.

The quantum geometry can be captured with the non-Abelian multiband quantum geometric tensor (QGT) [34], which reads,

$$(Q_{ab})_{\mu\nu} = \langle \partial^\mu a | 1 - \hat{P} | \partial^\nu b \rangle \quad (\text{A4})$$

where $\hat{P} = \sum_{\{c\}} |c\rangle \langle c|$ is a projector onto a set of bands. In the case of Hamiltonians with the non-trivial Euler invariant χ_{ab} , we choose to project onto the Euler bands,

$$\hat{P}_{\chi_{ab}} = |a\rangle \langle a| + |b\rangle \langle b|. \quad (\text{A5})$$

Due to the reality condition on the Hamiltonian $H(\mathbf{k}) = H^*(\mathbf{k})$, the eigenvectors can be chosen real $|a\rangle \in \mathbb{R}^N$, with N given by the number of the orbitals. Hence, the QGT is manifestly real, and reduces purely to its real part, the quantum metric $(g_{ab})_{\mu\nu} = \Re \mathfrak{e} (Q_{ab})_{\mu\nu}$,

$$(g_{ab})_{\mu\nu} = \frac{1}{2} \left(\langle \partial^\mu a | 1 - \hat{P} | \partial^\nu b \rangle + \langle \partial^\nu b | 1 - \hat{P} | \partial^\mu a \rangle \right). \quad (\text{A6})$$

Due to positive-semidefiniteness of QGT [45, 57, 68], one arrives at a bound between the quantum metric and the Euler curvature,

$$(g_{aa})_{xx} + (g_{bb})_{xx} + (g_{aa})_{yy} + (g_{bb})_{yy} \geq 2|\text{Eu}_{ab}|, \quad (\text{A7})$$

where we use the projector $\hat{P} = \hat{P}_{\chi_{ab}}$. In the context of this work, the quantum metric decomposes in terms of the interband matrix elements as,

$$(g_{aa})_{\mu\nu} = \sum_{c \neq b} \xi_{ac}^\mu \xi_{ca}^\nu, \quad (\text{A8})$$

with the intraband matrix elements $\xi_{aa}^\mu = 0$ vanishing under the reality condition. This allows to conclude with a geometric bound on the sum of the matrix elements entering the optical conductivities and higher-order responses studied diagrammatically in the following sections,

$$\sum_{c \neq b} \xi_{ac}^x \xi_{ca}^x + \sum_{c \neq a} \xi_{ac}^x \xi_{ca}^x + \sum_{c \neq b} \xi_{ac}^y \xi_{ca}^y + \sum_{c \neq b} \xi_{ac}^y \xi_{ca}^y \geq |\text{Eu}_{ab}|. \quad (\text{A9})$$

In the above, we showed how the Euler curvature provides a lower bound on the matrix elements corresponding to the transitions *from* and *to* Euler bands. Furthermore, we can consider the quantum geometry induced by the quadratic band touching hosting patch Euler class $\chi = 1$, and the resultant geometric conditions on the transition *between* the Euler bands. Within an effective $\mathbf{k} \cdot \mathbf{p}$ models for such node, it was shown in Ref. [45] that the multiband quantum metric for a rotationally-symmetric Euler nodes with patch invariant χ obtains,

$$\xi_{ab}^x \xi_{ba}^x + \xi_{ab}^y \xi_{ba}^y = \frac{\chi^2}{q^4} q^\mu q^\nu (2\delta_{\mu\nu} - 1), \quad (\text{A10})$$

where q is the momentum-space displacement from the position of the Euler node. We note that exactly at the node $q = 0$, the quantum metric formally diverges. Furthermore, we show that the presence of such momentum space singularity induces a quantized jump in the first-order optical conductivity (see App. D), as also discussed in the main text.

Appendix B: Phase difference and unconventional pairing in the Euler superconductor

Below we discuss the relationship between the order parameter phase difference in the band basis and the non-trivial pairing in orbital basis. We begin with the trivial coupling case of $\phi = 0$, which can be connected to the case $\Delta(\mathbf{k}) = \Delta_f \mathbb{1}_3$ assuming that $\Delta_+ = \Delta_f$ corresponds to purely an s -wave pairing. On the contrary, without changing the band structure (i.e. we keep $|\Delta_i| = \Delta_f$ for all bands), by setting the phase difference to $\phi = \pi$ between Δ_- and Δ_f (namely $\Delta_- = -\Delta_f$), with $\Delta_+ = \Delta_-$, we have a multiband order parameter:

$$\begin{aligned} \Delta(\phi = \pi) &= -\Delta_f \begin{pmatrix} 1 & 0 & 0 \\ 0 & \cos 2\theta & \sin 2\theta \\ 0 & \sin 2\theta & -\cos 2\theta \end{pmatrix} \\ &= -\Delta_f \oplus \frac{1}{r^2} (\Delta_{x^2-y^2} \tau_z - 2\Delta_{xy} \tau_x). \end{aligned} \quad (\text{B1})$$

Here, $\tan \theta = c_2/c_1$, and in the orbital basis, the order parameter can be written as a tensor sum of s -wave in A orbital, together with d -wave in B and C orbitals. As such, when we change the phase difference within the order parameter, we are effectively considering non-trivial pairing in the orbital basis, although there is no change in the band dispersion spectrum.

Appendix C: Generalized velocity operators

Below, for completeness, we show the computation of generalized velocity operator matrix elements in terms of the band dispersion and geometrical quantities [62, 65]. We begin with the non-Abelian multiband Berry connection

$$\xi_{ab}^\mu = i \langle a | \partial^\mu b \rangle, \quad (\text{C1})$$

which determines the matrix elements for the generalized operator (\mathcal{O}) derivatives:

$$\begin{aligned} \mathcal{O}_{ab}^\mu &= \langle a | \partial^\mu \mathcal{O} | b \rangle \\ &= \partial^\mu \langle a | \mathcal{O} | b \rangle - \langle \partial^\mu a | \mathcal{O} | b \rangle - \langle a | \mathcal{O} | \partial^\mu b \rangle \\ &= \partial^\mu \mathcal{O}_{ab} - \sum_c (\langle \partial^\mu a | c \rangle \langle c | \mathcal{O} | b \rangle + \langle a | \mathcal{O} | c \rangle \langle c | \partial^\mu b \rangle) \\ &= \partial^\mu \mathcal{O}_{ab} - \sum_c (i \xi_{ac}^\mu \mathcal{O}_{cb} - i \mathcal{O}_{ac} \xi_{cb}^\mu) \\ &= \partial^\mu \mathcal{O}_{ab} - i [\xi^\mu, \mathcal{O}]_{ab}. \end{aligned} \quad (\text{C2})$$

We first consider the case of a normal state with vanishing pairing terms, as introduced on the Lieb lattice in the main text. For the bulk Hamiltonian, derivative of which defines the velocity operator, we therefore have:

$$\begin{aligned} h_{ab}^\mu &= \partial^\mu h_{ab} - i [\xi^\mu, h]_{ab} \\ &= \partial^\mu \epsilon_a \delta_{ab} - i \xi_{ab}^\mu \epsilon_b + i \epsilon_a \xi_{ab}^\mu \\ &= \partial^\mu \epsilon_a \delta_{ab} + i \epsilon_{ab} \xi_{ab}^\mu. \end{aligned} \quad (\text{C3})$$

Furthermore, in the superconducting state, the velocity operator can be defined in terms of the velocity operator of the normal state:

$$\begin{aligned} J^{\mu_1 \dots \mu_n}(\mathbf{k}) &= (-1)^n \frac{\partial H(\mathbf{k}, \mathbf{A})}{\partial A_{\mu_1} \dots \partial A_{\mu_n}} \Big|_{\mathbf{A} \rightarrow 0} \\ &= \tau_z^{n+1} \otimes h^{\mu_1 \dots \mu_n}(\mathbf{k}). \end{aligned} \quad (\text{C4})$$

Correspondingly, in the band basis of the superconductor model introduced in the main text, we have:

$$\begin{aligned} J_{a,s_1;b,s_2}^{\mu_1 \dots \mu_n}(\mathbf{k}) &= \langle a, s_1 | J^{\mu_1 \dots \mu_n} | b, s_2 \rangle \\ &= \frac{(-1)^{n+1} + \alpha_{a,s_1}^* \alpha_{b,s_2}}{\sqrt{(1 + |\alpha_{a,s_1}|^2)(1 + |\alpha_{b,s_2}|^2)}} h_{ab}^{\mu_1 \dots \mu_n}(\mathbf{k}), \end{aligned} \quad (\text{C5})$$

which provides a convenient representation of the current operators for the diagrammatic calculations performed in the next Sections.

Appendix D: Linear response of Euler superconductors

Below we detail the calculation for linear response of an Euler, where we directly apply Eq. (G7). We begin by noting that due to the C_4 symmetry, and given the reality condition of the considered Hamiltonians, $\sigma^{\mu\nu}$ vanishes identically for $\mu \neq \nu$ in the considered models. As such the non-Drude part of the response, at zero temperature, is given by:

$$\sigma_{\text{Euler}} \equiv \sigma_{ab}^{\mu\mu} + \sigma_{ba}^{\mu\mu} = 2 \frac{i}{\omega} \int [d\mathbf{k}] \epsilon_{ab}^2 |\xi_{ab}^\mu|^2 \frac{(\tilde{\epsilon}_a + \tilde{\epsilon}_b)(\epsilon_a \epsilon_b - \tilde{\epsilon}_a \tilde{\epsilon}_b + \Delta_a \Delta_b \cos \phi)}{\tilde{\epsilon}_a \tilde{\epsilon}_b [(\tilde{\epsilon}_a + \tilde{\epsilon}_b)^2 - \omega^2]}. \quad (\text{D1})$$

We first consider a simplified case where only two bands are optically probed and relevant, and also assume $\epsilon_a = 0, \Delta_a = \Delta_b$. Having further assumed no angular dependence for band dispersion, we have the following:

$$\begin{aligned} \sigma_{\text{Euler}} &\sim \frac{2i}{\omega A} \int_0^{r_0} \int_0^{2\pi} r dr d\theta \frac{(\Delta_a + \tilde{\epsilon}_b)(-\Delta_a \tilde{\epsilon}_b + \Delta_a^2 \cos \phi)}{\Delta_a \tilde{\epsilon}_b [(\Delta_a + \tilde{\epsilon}_b)^2 - \omega^2]} \epsilon_j^2 |\xi_{ab}^\mu|^2 \\ &= -\frac{2i}{\omega A} \int_{2\Delta_a}^{E_0} \int_0^{2\pi} r dE d\theta \left(\frac{d\tilde{\epsilon}_b}{dr} \right)^{-1} \frac{E[E - \Delta_a(1 + \cos \phi)]}{\tilde{\epsilon}_b(E^2 - \omega^2)} \epsilon_j^2 |\xi_{ab}^\mu|^2 \\ &= -\frac{2i}{\omega A} \int_{2\Delta_a}^{E_0} \int_0^{2\pi} r dE d\theta \left(\frac{1}{\epsilon_b} \frac{d\epsilon_b}{dr} \right)^{-1} \frac{E[E - \Delta_a(1 + \cos \phi)]}{E^2 - \omega^2} |\xi_{ab}^\mu|^2 \\ &\sim -\frac{2i}{\omega A} \int_0^{2\pi} d\theta f^2(\theta) \int_{2\Delta_a}^{E_0} dE \frac{r^{2(1+n)}}{m} \frac{E[E - \Delta_a(1 + \cos \phi)]}{E^2 - \omega^2}, \end{aligned} \quad (\text{D2})$$

where $E = \Delta_a + \tilde{\epsilon}_b$, A is the area of the BZ, and in the third line, we make an Ansatz $|\xi_{ab}^\mu|^2 \sim r^{2n} f^2(\theta)$ and $\epsilon_b \sim \alpha r^m$, locally around the node. The Ansatz follows from considering a minimal effective $\mathbf{k} \cdot \mathbf{p}$ model for an Euler superconductor,

$$H_{\text{SC}}^\chi(\mathbf{k}) = \begin{pmatrix} H^\chi(\mathbf{k}) & \Delta_i \mathbf{1}_2 \\ \Delta_i \mathbf{1}_2 & -H^\chi(\mathbf{k}) \end{pmatrix} = \alpha(k_x^2 + k_y^2)[\mathbf{1}_2 \otimes \tau_z] + \begin{pmatrix} 2\alpha k_x k_y & \alpha(k_x^2 - k_y^2) & \Delta_i & 0 \\ \alpha(k_x^2 - k_y^2) & -2\alpha k_x k_y & 0 & \Delta_i \\ \Delta_i & 0 & -2\alpha k_x k_y & \alpha(k_y^2 - k_x^2) \\ 0 & \Delta_i & \alpha(k_y^2 - k_x^2) & 2\alpha k_x k_y \end{pmatrix}, \quad (\text{D3})$$

where ' \otimes ' denotes a Kronecker product, and the first term only contributes to the appropriate quadratic or flat band band dispersions. The Hamiltonian above corresponds to the case in which the phase difference is $\phi = 0$. The non-zero phase difference can be introduced with non-trivial pairing, as detailed in App. B. In the above, the nodal Hamiltonian $H^\chi(\mathbf{k})$ in the individual particle and hole sectors more compactly reads [26, 53]:

$$H^\chi(\mathbf{k}) = \alpha[(k_x^2 + k_y^2)\mathbf{1}_2 + (k_x^2 - k_y^2)\tau_x + 2k_x k_y \tau_z]. \quad (\text{D4})$$

We note that the form of dispersion controlled by α only contributes to the prefactor of the integral and to the eigenstate normalization factors, which cancel, as $n = -1$ for the quadratic node with Euler class $\chi = 1$ that is centered around $r = 0$ [45]. Specifically in the case of a single quadratic Euler node, we retrieve $f(\theta) = \chi \sin \theta$ from the eigenstates [45], and we have:

$$\sigma_{\text{Euler}} = -\frac{2i\pi\chi^2}{m\omega A} \int_{2\Delta_i}^{E_0} dE \frac{E[E - \Delta_i(1 + \cos \phi)]}{E^2 - \omega^2} \quad (\text{D5})$$

$$\begin{aligned} \Re[\sigma_{\text{Euler}}(2\Delta_f < \omega < E_0)] &\sim -\frac{2i\pi\chi^2}{4\pi^2 m\omega} (-\pi i) \frac{\omega[\omega - \Delta_i(1 + \cos \phi)]}{2\omega} \\ &= -\frac{\chi^2}{4m} \left(1 - \frac{\Delta_i}{\omega}(1 + \cos \phi) \right) \end{aligned} \quad (\text{D6})$$

$$\begin{aligned} \Im[\sigma_{\text{Euler}}(\omega)] &= -\frac{2\pi\chi^2}{m\omega A} \Re \left(E - \frac{\omega}{2} \ln \frac{\omega + E}{\omega - E} - \Delta_i \frac{1 + \cos \phi}{2} \ln(E^2 - \omega^2) \right) \Big|_{E=2\Delta_i}^{E_0} \\ \Im[\sigma_{\text{Euler}}(\omega \sim 2\Delta_i)] &\sim \begin{cases} -\frac{\pi\chi^2}{2mA} (1 - \cos \phi) \ln |2\Delta_i - \omega| & \text{for } \phi \neq 0 \\ \frac{\pi\chi^2}{mA} \left(2 + 2 \ln \frac{2\Delta_0 + E_0}{4\Delta_0} - \frac{E_0}{\Delta_0} \right) & \text{for } \phi = 0 \end{cases} \end{aligned} \quad (\text{D7})$$

$$\Im [\sigma_{\text{Euler}}(\omega \sim E_0)] \sim -\frac{\pi\chi^2}{mE_0A} [E_0 - \Delta_0(1 + \cos\phi)] \ln |E_0 - \omega|. \quad (\text{D8})$$

In the above, we set $A = (2\pi)^2$ when calculating the real part. The real part vanishes outside of $2\Delta_f < \omega < E_0$, and at $\omega \sim 2\Delta_f$ we have a simplified form $\Re [\sigma_{\text{Euler}}] = -\chi^2(1 - \cos\phi)/4m$. For the imaginary part, at $\omega \sim 2\Delta_i$, which corresponds to the transition between Euler nodes in different sectors, there is a divergent peak, except when $\phi = 0$.

Below we further check with the exact form of an eigensystem of our concrete model (see Sec. II). When the third band is isolated, only the transition between the flat band to the neighboring dispersive band could give rise to a response. We thus have $\epsilon_a = 0$, $\epsilon_b = \epsilon_-$, $\tilde{\epsilon}_a = \Delta_f$, $\tilde{\epsilon}_b = \sqrt{\Delta_f^2 + \epsilon_-^2}$, $|\xi_{ab}|^2 = (\sin^2\theta, \cos^2\theta)/(r^2 + \epsilon_-^2)$. We can substitute back into Eq. (D1), which gives:

$$\sigma_{\text{Euler}} = \frac{2i\pi}{\omega A} \int_0^{r_0} r dr \frac{\epsilon_-^2}{r^2 + \epsilon_-^2} \frac{(\Delta_f + \sqrt{\Delta_f^2 + \epsilon_-^2}) (-\Delta_f \sqrt{\Delta_f^2 + \epsilon_-^2} + \Delta_f^2 \cos\phi)}{\Delta_f \sqrt{\Delta_f^2 + \epsilon_-^2} \left[(\Delta_f + \sqrt{\Delta_f^2 + \epsilon_-^2})^2 - \omega^2 \right]} \quad (\text{D9})$$

$$= -\frac{i\pi}{\omega A} \int_{2\Delta_f}^{E_0} dE \frac{E[E - \Delta_0(1 + \cos\phi)]}{E^2 - \omega^2}, \quad (\text{D10})$$

where $E_0 = \Delta_f + \sqrt{\Delta_f^2 + \epsilon_-^2}(r_0)$. Note the function form is identical to that of $m = 2$ corresponding to the quadratic dispersion, thus result can be retrieved by substituting $m = 2$ into Eq. (D6-D8). In particular, we note the quantized optical conductivity jump of $e^2/(8\hbar)$ at $\omega \sim 2\Delta_0$, which was identified and discussed in the main text for $\phi = \pi$.

Appendix E: Decomposition and analysis of parity effects

We briefly comment on the effects of parity breaking, in particular focusing on the second-order optical responses. We begin by recognizing that, given a Hamiltonian $h(\mathbf{k})$, we can decompose it in terms of its even ($e(\mathbf{k})$) and odd ($o(\mathbf{k})$) parts:

$$h(\mathbf{k}) = o(\mathbf{k}) + e(\mathbf{k}), \quad (\text{E1})$$

$$o(-\mathbf{k}) = -o(\mathbf{k}), \quad (\text{E2})$$

$$e(-\mathbf{k}) = e(\mathbf{k}). \quad (\text{E3})$$

We now employ a parity-based decomposition to the generalized velocity operators (see also App. B), which obtains

$$\begin{aligned} J^{\mu_1 \dots \mu_n}(\mathbf{k}) &= (-1)^n \prod_{i=1}^n \frac{\partial}{\partial A^{\mu_i}} H(\mathbf{k}, \mathbf{A}) \Big|_{\mathbf{A} \rightarrow 0} \\ &= \tau_3^n \begin{pmatrix} j(\mathbf{k}) & 0 \\ 0 & -j(-\mathbf{k}) \end{pmatrix} \\ &= \tau_3^n \left[\begin{pmatrix} j_e^{\mu_1 \dots \mu_n}(\mathbf{k}) & 0 \\ 0 & -j_e^{\mu_1 \dots \mu_n}(\mathbf{k}) \end{pmatrix} + \begin{pmatrix} j_o^{\mu_1 \dots \mu_n}(\mathbf{k}) & 0 \\ 0 & j_o^{\mu_1 \dots \mu_n}(\mathbf{k}) \end{pmatrix} \right] \end{aligned} \quad (\text{E4})$$

$$= \begin{cases} \tau_3 \otimes j_e^{\mu_1 \dots \mu_n} + \mathbb{1}_2 \otimes j_o^{\mu_1 \dots \mu_n} & n \text{ is even} \\ \tau_3 \otimes j_o^{\mu_1 \dots \mu_n} + \mathbb{1}_2 \otimes j_e^{\mu_1 \dots \mu_n} & n \text{ is odd} \end{cases}, \quad (\text{E5})$$

where we define $j_o^\mu = \langle a | \partial^\mu o | b \rangle$ and $j_e^\mu = \langle a | \partial^\mu e | b \rangle$. Thus, in the BdG band basis, we have:

$$\begin{aligned} J_{2,-;2,+}^\mu &= \frac{(\alpha_{2,-}\alpha_{2,+} - 1)j_o^\mu + (\alpha_{2,-}\alpha_{2,+} + 1)j_e^\mu}{\sqrt{(1 + |\alpha_{2,-}|^2)(1 + |\alpha_{2,+}|^2)}} \\ &= -\frac{\Delta_i}{\sqrt{\Delta_i^2 + \epsilon_e^2}} \partial^\mu \epsilon_o \end{aligned} \quad (\text{E6})$$

$$\begin{aligned} J_{2,p;2,p}^\mu &= \frac{(|\alpha_{2,p}|^2 - 1)j_o^\mu + (|\alpha_{2,p}|^2 + 1)j_e^\mu}{1 + |\alpha_{2,p}|^2} \\ &= j_e^\mu + \frac{p\epsilon_e}{\sqrt{\Delta_i^2 + \epsilon_e^2}} j_o^\mu \end{aligned} \quad (\text{E7})$$

$$\Delta_{y,+;2,-}^{\mu} = \frac{2\epsilon_e}{\sqrt{\Delta_i^2 + \epsilon_e^2}} j_o^{\mu}. \quad (\text{E8})$$

Therefore, as the main second-order response is due to the $-, - \rightarrow -, +$ processes, the optical conductivity at the second order in electric fields does not depend on the quantum geometry of the normal state, but only on the dispersion. Hence, unlike the first-order response, the second-order response cannot be directly used to target and infer the topological Euler invariant.

Appendix F: Selection rules for the Euler nodes in superconductors

In the following, we discuss an emergent selection rule exactly at the node, which is due to the vertex contribution $J_{a,s_1;b,s_2}^{\mu_1 \dots \mu_n}$. Here, a, b are band indices, and $s_1, s_2 = \pm 1$ are sector indices, with $+1$ (-1) corresponding to electron (hole) sectors. We note that the eigenstate of the BdG Hamiltonian can be decomposed as tensor product between the Nambu basis and the band basis:

$$|a; s_1\rangle = |a, s_1\rangle \otimes |a\rangle, \quad (\text{F1})$$

$$|a, s_1\rangle = \frac{1}{\sqrt{2}} \begin{pmatrix} s_1 e^{i\phi_i} \\ 1 \end{pmatrix}. \quad (\text{F2})$$

Similarly, we can decompose the coupling at the vertex, see Fig. 6, as:

$$\begin{aligned} J_{a,s_1;b,s_2}^{\mu_1 \dots \mu_n} &= h_{a,b}^{\mu_1 \dots \mu_n} \langle a, s_1 | \tau_z^{n+1} | b, s_2 \rangle \\ &= \frac{1}{2} h_{a,b}^{\mu_1 \dots \mu_n} [(-1)^{n+1} + s_1 s_2 e^{i\Delta\phi}]. \end{aligned} \quad (\text{F3})$$

Two interesting cases arise when $\Delta\phi = \phi_2 - \phi_1 = 0, \pi$, where certain vertices vanish depending on whether the transition is of inter- or intra- sector kind. These selection rules, for the vanishing of the coupling to the current operator at the vertex, can be summarized as:

n	$\Delta\phi$	Sector	Selection rules
Odd	0	Intra	✓
		Inter	✗
	π	Intra	✗
		Inter	✓
Even	0	Intra	✗
		Inter	✓
	π	Intra	✓
		Inter	✗

(F4)

Note that the selection rule for band indices $i = j$ is the same as for when $\Delta\phi = 0$.

Appendix G: Diagrammatic approach to the superconducting state

We hereby provide a calculation of the optical responses of Euler superconductors within the diagrammatic approach [65].

The BdG Hamiltonian with \mathcal{PT} symmetry, and specifically, with intraband pairing interactions, can be decomposed as:

$$H(\mathbf{k}) = \sum_a \begin{pmatrix} \epsilon_a(\mathbf{k}) & \Delta_a(\mathbf{k}) \\ \Delta_a^*(\mathbf{k}) & -\epsilon_a(\mathbf{k}) \end{pmatrix} \otimes P_a(\mathbf{k}), \quad (\text{G1})$$

where P_l is the projector matrix to band l in normal state. Diagrammatically, as shown in Fig. 6, the total first-order photoconductivity is given by [65, 66]:

$$\sigma^{\mu\nu}(\omega) = \frac{i}{\omega} \int [d\mathbf{k}] \int dk_0 \text{Tr}[J^{\mu\nu} G(k_0) + J^{\mu} G(k_0 + \omega) J^{\nu} G(k_0)]., \quad (\text{G2})$$

The Green's function $G^{-1}(k_0, \mathbf{k}) = k_0 - H(\mathbf{k})$ can be rewritten as:

$$\begin{aligned} G(k_0, \mathbf{k}) &= \sum_a \begin{pmatrix} k_0 - \epsilon_a(\mathbf{k}) & -\Delta_a(\mathbf{k}) \\ -\Delta_a^*(\mathbf{k}) & k_0 + \epsilon_a(\mathbf{k}) \end{pmatrix}^{-1} \otimes P_a \\ &= \sum_a G_a(k_0, \mathbf{k}) \otimes P_a \end{aligned} \quad (\text{G3})$$

$$G_i(k_0, \mathbf{k}) = \frac{1}{\omega_0^2 - \tilde{\epsilon}_a^2} \begin{pmatrix} k_0 + \epsilon_a & \Delta_a \\ \Delta_a^* & k_0 - \epsilon_a \end{pmatrix}. \quad (\text{G4})$$

Furthermore, as the velocity operators can be decomposed as $J^{\mu\nu} = \tau_z \otimes h^{\mu\nu}$ and $J^\mu = I_2 \otimes h^{\mu\nu}$, we have:

$$\begin{aligned} \sigma^{\mu\nu}(\omega) &= \frac{i}{\omega} \int [d\mathbf{k}] \int dk_0 \text{Tr}[J^{\mu\nu} G(k_0) + J^\mu G(k_0 + \omega) J^\nu G(k_0)] \\ &= \frac{i}{\omega} \sum_{a,b} \int [d\mathbf{k}] \int dk_0 \{h_{aa}^{\mu\nu} \text{Tr}[\tau_z G_a(k_0)] + h_{ab}^\mu h_{ba}^\nu \text{Tr}[G_b(k_0 + \omega) G_a(k_0)]\} \\ &= \frac{i}{\omega} \sum_{a,b} \int [d\mathbf{k}] [h_{aa}^{\mu\nu} \tilde{I}_1 + h_{ab}^\mu h_{ji}^\nu \tilde{I}_2(\omega)], \end{aligned} \quad (\text{G5})$$

where these integrals are calculated in App. I. We note that the form is identical to the normal state, with the velocity operator inherited from the normal state, up to the correction that is included within the integral. Moreover, this can be computed explicitly at zero temperature:

$$\frac{i}{\omega} \int [d\mathbf{k}] h_{aa}^{\mu\nu} \tilde{I}_1 \sim -\frac{i}{\omega} \int [d\mathbf{k}] \partial^\mu \partial^\nu \epsilon_a \frac{\epsilon_a}{\sqrt{\Delta_a^2 + \epsilon_a^2}} \quad (\text{G6})$$

$$\begin{aligned} \frac{i}{\omega} \int [d\mathbf{k}] h_{ab}^\mu h_{ba}^\nu \tilde{I}_2(\omega) &\sim \frac{i}{\omega} \int [d\mathbf{k}] \epsilon_{ab}^2 \xi_{ab}^\mu \xi_{ba}^\nu \frac{(\tilde{\epsilon}_a + \tilde{\epsilon}_b)(\epsilon_a \epsilon_b - \tilde{\epsilon}_a \tilde{\epsilon}_b + \Delta_a \Delta_b \cos \phi)}{\tilde{\epsilon}_a \tilde{\epsilon}_b [(\tilde{\epsilon}_a + \tilde{\epsilon}_b)^2 - \omega^2]} \\ &= -\frac{i}{\omega} \int [d\mathbf{k}] \epsilon_{ab}^2 \xi_{ab}^\mu \xi_{ab}^\nu \frac{(\tilde{\epsilon}_a + \tilde{\epsilon}_b)(\epsilon_a \epsilon_b - \tilde{\epsilon}_a \tilde{\epsilon}_b + \Delta_a \Delta_b \cos \phi)}{\tilde{\epsilon}_a \tilde{\epsilon}_b [(\tilde{\epsilon}_a + \tilde{\epsilon}_b)^2 - \omega^2]}. \end{aligned} \quad (\text{G7})$$

Appendix H: Third-order conductivity

Within a further application of the diagrammatic techniques demonstrated in the approach summarized in the previous section (App. G), we can deduce the third-order conductivity:

$$\begin{aligned} &\sigma^{\mu\nu\rho\lambda}(\omega; \omega_1, \omega_2, \omega_3) \\ &= -\frac{i}{3! \omega_1 \omega_2 \omega_3} \sum_a \int [d\mathbf{k}] \int dk_0 G_a(k_0) J_{aa}^{\mu\nu\rho\lambda} \\ &\quad - \frac{i}{2! \omega_1 \omega_2 \omega_3} \sum_a \int [d\mathbf{k}] \int dk_0 G_a(k_0) J_{ab}^\nu G_b(k_0 + \omega_1) J_{ba}^{\mu\rho\lambda} \\ &\quad - \frac{i}{2! \omega_1 \omega_2 \omega_3} \sum_a \int [d\mathbf{k}] \int dk_0 G_a(k_0) J_{ab}^{\nu\rho} G_b(k_0 + \omega_{12}) J_{ba}^{\mu\lambda} \\ &\quad - \frac{i}{3! \omega_1 \omega_2 \omega_3} \sum_a \int [d\mathbf{k}] \int dk_0 G_a(k_0) J_{ab}^{\nu\rho\lambda} G_b(k_0 + \omega_{123}) J_{ba}^\mu \\ &\quad - \frac{i}{\omega_1 \omega_2 \omega_3} \sum_a \int [d\mathbf{k}] \int dk_0 G_a(k_0) J_{ab}^\nu G_b(k_0 + \omega_1) J_{bc}^\rho G_c(k_0 + \omega_{12}) J_{ca}^{\mu\lambda} \\ &\quad - \frac{i}{2! \omega_1 \omega_2 \omega_3} \sum_a \int [d\mathbf{k}] \int dk_0 G_a(k_0) J_{ab}^\nu G_b(k_0 + \omega_1) J_{bc}^{\rho\lambda} G_c(k_0 + \omega_{123}) J_{ca}^\mu \\ &\quad - \frac{i}{2! \omega_1 \omega_2 \omega_3} \sum_a \int [d\mathbf{k}] \int dk_0 G_a(k_0) J_{ab}^{\nu\rho} G_b(k_0 + \omega_{12}) J_{bc}^\lambda G_c(k_0 + \omega_{123}) J_{ca}^\mu \end{aligned}$$

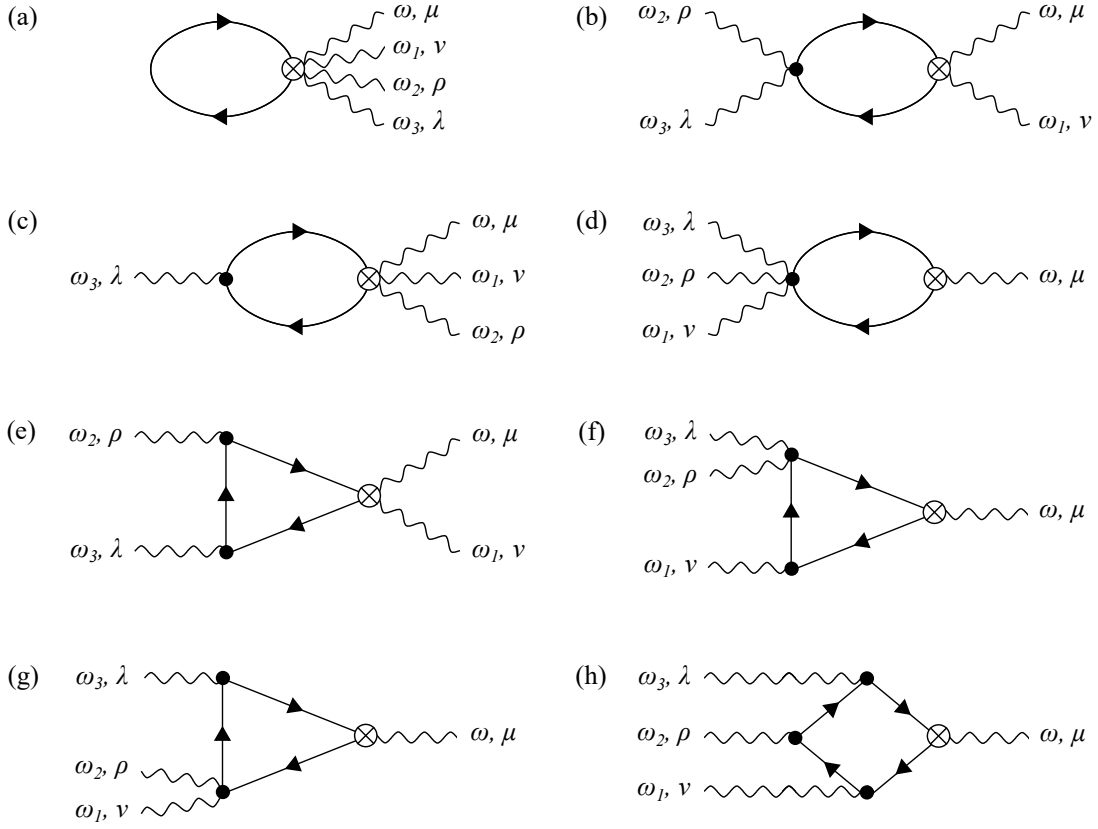


FIG. 7. List of possible diagrams for third-order optical responses. In main text, we have only discussed the four-vertex diagram (h), since it is the only diagram that majorly contributes to the optical response of an Euler superconductor.

$$-\frac{i}{\omega_1\omega_2\omega_3} \sum_a \int [d\mathbf{k}] \int dk_0 G_a(k_0) J_{ab}^\nu G_b(k_0 + \omega_1) J_{bc}^\rho G_c(k_0 + \omega_{12}) J_{cd}^\lambda G_d(k_0 + \omega_{123}) J_{da}^\mu,$$

which needs to be symmetrized with respect to all permutations $\nu, \omega_1; \rho, \omega_2; \lambda, \omega_3$. As discussed in the main text, we are interested in the last term, which corresponds to the diagram Fig. 7(h). In particular, choosing $\phi = \pi$, for $\mu = \nu = \rho = \lambda = x$ and $\omega = \omega_1 = \omega_3 = -\omega_2$, with $\omega > 0$, only the following two processes are important: $f, - \rightarrow -, + \rightarrow f, - \rightarrow -, + \rightarrow f, -$ and $-, - \rightarrow f, + \rightarrow -, - \rightarrow f, + \rightarrow -, -$. The corresponding photoconductivity contributions are given by:

$$-\frac{2}{3} \frac{i}{\omega^3} \int [d\mathbf{k}] \int dk_0 G_{-,-}(k_0) J_{-,-;f,+}^x G_{f,+}(k_0 + \omega) J_{f,+;-}^x G_{-,-}(k_0) J_{-,-;f,+}^x G_{f,+}(k_0 + \omega) J_{f,+;-}^x, \quad (\text{H1})$$

where the factor of 2 is due to two individual processes, and the factor of 1/3 is due to the symmetrization with respect to all permutations. In particular, on setting the zero temperature limit, this simplifies to the following integral [66]:

$$\begin{aligned} I_4 &= \int dk_0 G_{-,-}(k_0) G_{f,+}(k_0 + \omega) G_{-,-}(k_0) G_{f,+}(k_0 + \omega) \\ &= \frac{1}{2i\eta(-\tilde{\epsilon}_- - \Delta_0 + \omega + i\eta)(-\tilde{\epsilon}_- - \Delta_0 + \omega + 3i\eta)} + \frac{1}{-2i\eta(-\tilde{\epsilon}_- - \Delta_0 + \omega + i\eta)(-\tilde{\epsilon}_- - \Delta_0 + \omega - i\eta)} \\ &= \frac{1}{(\tilde{\epsilon}_- + \Delta_0 - \omega + i\eta)(-\tilde{\epsilon}_- - \Delta_0 + \omega + i\eta)(-\tilde{\epsilon}_- - \Delta_0 + \omega + 3i\eta)}. \end{aligned} \quad (\text{H2})$$

In the context of the photoconductivity contributions specified above, recall that the velocity operator is given by:

$$J_{-,-;f,+}^x = \frac{1}{\sqrt{2}} \frac{\Delta_0 - \epsilon_- + \tilde{\epsilon}_-}{\sqrt{\Delta_0^2 + (\epsilon_- - \tilde{\epsilon}_-)^2}} j_{f,-}^x(\mathbf{k}), \quad (\text{H3})$$

which results in:

$$\begin{aligned}\sigma^{xxxx} &\sim -\frac{2}{3} \frac{i}{\omega^3} \int [d\mathbf{k}] \frac{I_4}{4} \left(\frac{\Delta_0 - \epsilon_- + \tilde{\epsilon}_-}{\sqrt{\Delta_0^2 + (\epsilon_- - \tilde{\epsilon}_-)^2}} \right)^4 \epsilon_-^4 |\xi_{f-}^x|^4 \\ &\sim -\frac{2}{3} \frac{i}{\omega^3 A} \int_0^{r_0} \int_0^{2\pi} r dr d\theta 2I_4 \alpha^4 r^{4m-4} \chi^4 \sin^4 \theta.\end{aligned}\quad (\text{H4})$$

We further apply the $\mathbf{k} \cdot \mathbf{p}$ model-based Ansatz: $|\xi_{ij}^\mu|^2 \sim r^{-2} \chi^2 \sin^2 \theta$, and $\epsilon_j \sim \alpha r^m$ (see App. D), locally around the node, as also previously detailed in the linear conductivity calculation of App. G. We note that the result depends on the value of m , or equivalently, on the profiles of the band dispersions, and depends on the quasiparticle relaxation rate η . For example, for $m = 2$, i.e., for a quadratic band, we have $\sigma^{xxxx} \propto 1/\eta^2$, and:

$$\begin{aligned}\sigma^{xxxx} &\sim -\frac{2}{3} \frac{i}{\omega^3 A} \int_0^{r_0} \int_0^{2\pi} r dr d\theta \frac{2\alpha^4 r^4 \chi^4 \sin^4 \theta}{\eta^2 (\omega - \Delta_0 - \sqrt{\Delta_0^2 + \alpha^2 r^4})} \\ &\sim -\frac{2}{3} \frac{i}{\omega^3 A} \int_0^{\epsilon_0} \int_0^{2\pi} d\epsilon d\theta \frac{2\alpha \epsilon^2 \chi^4 \sin^4 \theta}{m\eta^2 (\omega - \Delta_0 - \sqrt{\Delta_0^2 + \epsilon^2})} \\ \Re[\sigma^{xxxx}] &\propto \frac{\chi^4}{\eta^2} \sqrt{\omega - 2\Delta_0} \quad \text{for } \omega > 2\Delta_0.\end{aligned}\quad (\text{H5})$$

We note that distinctly from the linear response, there is a dependence on $\eta \sim 1/\tau$ where τ is the relaxation time for the photoexcited particle to decay. Consistently with our numerical findings, we thus note that the transition is no longer a discrete jump but instead evolves into a continuous increase.

Appendix I: Useful integral

Below we discuss integrating over the trace of product of Green's function of the BdG Hamiltonian, with Green's function defined by (G4), which is particularly useful in the context of the integrals performed within the diagrammatic approach (App. G) applied to the considered superconductors [65]. In particular, at finite temperature, the integral can be related to the Matsubara sum of odd frequency $\omega_n = (2n + 1)\pi/\beta$ for $n \in \mathbb{Z}$. For example:

$$\begin{aligned}\tilde{I}_1 &= \int d\omega \text{Tr}[\tau_z G_a(\omega)] \\ &= \int d\omega \frac{2\epsilon_a}{\omega^2 - \tilde{\epsilon}_a^2} \\ &= -\frac{1}{\beta} \sum_n \frac{2\epsilon_a}{\tilde{\epsilon}_a^2 + \omega_n^2} \\ &= f(\tilde{\epsilon}_a) R_1(\tilde{\epsilon}_a) + f(-\tilde{\epsilon}_a) R_1(-\tilde{\epsilon}_a) \\ &= -\frac{\epsilon_a}{\tilde{\epsilon}_a} \tanh \frac{\beta \tilde{\epsilon}_a}{2},\end{aligned}\quad (\text{I1})$$

where R_1 is the residue of the integrand of \tilde{I}_1 . Similarly, we have:

$$\begin{aligned}\tilde{I}_2 &= \int d\omega \text{Tr}[G_a(\omega) G_b(\omega + \omega_1)] \\ &= \int d\omega \frac{\Delta_a^* \Delta_b + \Delta_a \Delta_b^* + 2\epsilon_a \epsilon_b + 2\omega(\omega + \omega_1)}{(\omega^2 - \tilde{\epsilon}_a^2)[(\omega + \omega_1)^2 - \tilde{\epsilon}_b^2]} \\ &= 2 \int d\omega \frac{\Delta_a \Delta_b \cos \phi + \epsilon_a \epsilon_b + \omega(\omega + \omega_1)}{(\omega^2 - \tilde{\epsilon}_a^2)[(\omega + \omega_1)^2 - \tilde{\epsilon}_b^2]}.\end{aligned}\quad (\text{I2})$$

Note that ω_1 corresponds to the photon (i.e. bosonic) degrees of freedom, thus it is governed by the even Matsubara frequency $2m\pi/\beta$ for $m \in \mathbb{Z}$. In the last line, we have also used ϕ to represent the phase between the order parameter (see App. C), and Δ_a now refers to the modulus of the order parameter. The integral can be analytically continued to sum over the odd Matsubara frequencies z :

$$\tilde{I}_2 = \frac{2}{\beta} \sum_z \frac{\Delta_a \Delta_b \cos \phi + \epsilon_a \epsilon_b - z(z + i\omega_1)}{(z^2 - \tilde{\epsilon}_a^2)[(z + i\omega_1)^2 - \tilde{\epsilon}_b^2]}$$

$$\begin{aligned}
&= \sum_{z=\pm\tilde{\epsilon}_a, \pm\tilde{\epsilon}_b - i\omega_1} f(z)R_2(z) \\
&= \frac{(\tilde{\epsilon}_a + \tilde{\epsilon}_b)(\epsilon_a\epsilon_b - \tilde{\epsilon}_a\tilde{\epsilon}_b + \Delta_a\Delta_b \cos\phi)}{\tilde{\epsilon}_a\tilde{\epsilon}_b[(\tilde{\epsilon}_a + \tilde{\epsilon}_b)^2 - \omega_1^2]} [f(-\tilde{\epsilon}_a) - f(\tilde{\epsilon}_b)] - \frac{(\tilde{\epsilon}_a - \tilde{\epsilon}_b)(\epsilon_a\epsilon_b + \tilde{\epsilon}_a\tilde{\epsilon}_b + \Delta_a\Delta_b \cos\phi)}{\tilde{\epsilon}_a\tilde{\epsilon}_b[(\tilde{\epsilon}_a - \tilde{\epsilon}_b)^2 - \omega_1^2]} [f(-\tilde{\epsilon}_a) - f(-\tilde{\epsilon}_b)],
\end{aligned} \tag{I3}$$

where the first term corresponds to the intersector processes, whereas the second term corresponds to the intrasector processes. In particular, at zero temperature, with the band i being flat, $\Delta_a = \Delta_b$, and $\epsilon_b \ll \Delta_a$; we have:

$$\begin{aligned}
\tilde{I}_2 &= \frac{(\Delta_a + \tilde{\epsilon}_b)(-\tilde{\epsilon}_b + \Delta_a \cos\phi)}{\tilde{\epsilon}_b[(\Delta_a + \tilde{\epsilon}_b)^2 - \omega_1^2]} \\
&= \frac{\Delta_a(1 - \cos\phi)}{\omega_1^2 - 4\Delta_a^2} + \frac{4\Delta_a^2 + \omega_1^2 - 12\Delta_a^2 \cos\phi + \omega_1^2 \cos\phi}{4\Delta_a(\omega_1^2 - 4\Delta_a^2)^2} \epsilon_b^2 + O(\epsilon_b^3),
\end{aligned} \tag{I4}$$

while the intrasector contribution vanishes. We note that this form can be further simplified for $\omega_1 \sim 2\Delta_a$:

$$\tilde{I}_2 \sim \frac{\Delta_a(1 - \cos\phi)}{\omega_1^2 - 4\Delta_a^2} + \frac{2\Delta_a(1 - \cos\phi)}{(\omega_1^2 - 4\Delta_a^2)^2} \epsilon_b^2 + O(\epsilon_b^3), \tag{I5}$$

which is proportional to $(1 - \cos\phi)$ up to the second order in ϵ_b , consistently with our findings that were numerically retrieved in the main text, and furthermore, analytically derived in the previous sections.

Appendix J: Allowed processes in third-order optical responses of Euler superconductors

We now detail the selection rules for the allowed third-order processes in the optical responses of the studied Euler superconductors. Based on all the possible selection rules, derived analogously to App. F, we note that only the following transitions have significant contributions. Namely, for $\Delta\phi = 0$, we have:

$$\begin{aligned}
&1- \rightarrow 2- \rightarrow 2- \rightarrow 2- \rightarrow 1- \\
&1- \rightarrow 2- \rightarrow 2- \rightarrow 1- \rightarrow 1- \quad (3 \text{ Permutations}) \\
&1- \rightarrow 2- \rightarrow 1- \rightarrow 1- \rightarrow 1- \quad (3 \text{ Permutations}) \\
&1- \rightarrow 1- \rightarrow 1- \rightarrow 1- \rightarrow 1- \\
&1- \Rightarrow 2+ \rightarrow 1+ \not\rightarrow 1- \\
&1- \Rightarrow 2+ \rightarrow 2+ \not\rightarrow 1- \\
&1- \Rightarrow 1+ \rightarrow 1+ \not\rightarrow 1- \\
&1- \Rightarrow 1+ \rightarrow 2+ \not\rightarrow 1- \\
&1- \Rightarrow 2+ \Rightarrow 1- \\
&1- \Rightarrow 1+ \Rightarrow 1- \\
&1- \Rightarrow 2- \rightarrow 1- \\
&1- \Rightarrow 1- \rightarrow 1- \\
&1- \rightarrow 1-
\end{aligned}$$

Here, \rightarrow represents a process with a single photon vertex (see Fig. 7), \Rightarrow for a two photon vertex, and \Rightarrow for a three photon vertex [Fig. 7(c,d)]. In the last line, presented is a process with a single vertex of four photons [Fig. 7(a)]. We denote the suppressed processes with $\not\rightarrow$. Similarly we can list down the relevant transitions for $\Delta\phi = \pi$:

$$\begin{aligned}
&1- \rightarrow 2+ \rightarrow 1- \rightarrow 2+ \rightarrow 1- \quad (3 \text{ Permutations}) \\
&1- \rightarrow 1- \rightarrow 1- \rightarrow 1- \rightarrow 1- \\
&1- \Rightarrow 2- \rightarrow 1+ \not\rightarrow 1- \\
&1- \Rightarrow 2- \rightarrow 2- \not\rightarrow 1- \\
&1- \Rightarrow 1+ \rightarrow 1+ \not\rightarrow 1- \\
&1- \Rightarrow 1+ \rightarrow 2- \not\rightarrow 1- \\
&1- \Rightarrow 2- \Rightarrow 1-
\end{aligned}$$

$$\begin{aligned}
1- &\Rightarrow 1+ \Rightarrow 1- \\
1- &\Rightarrow 2+ \rightarrow 1- \\
1- &\Rightarrow 1- \rightarrow 1- \\
1- &\rightarrow 1-
\end{aligned}$$

We note that all the optical transition processes between the Euler nodes that correspond to the jerk current [67] are suppressed for both $\Delta\phi = 0$ and $\Delta\phi = \pi$. The jerk-like current contributions, i.e. diagrams with two vertices of one photon, and one vertex of two photons, with the two-photon transition being between the Euler bands, including a returning transition, is vanishing, unless a band other than the bands hosting the Euler class is involved.

Appendix K: Vertex correction

We hereby comment on the diagrammatic computation of the vertex correction, which is intrinsic to the optical responses of the considered superconductors. The importance of the vertex correction within a diagrammatic approach to the optical responses of superconductors was addressed in Ref. [65], where the calculation was performed in the sublattice/orbital basis. Below, we will follow an analogous formalism, but instead use the band basis, which allows for a simpler decomposition. More specifically, we have an interaction Hamiltonian of form $H_{\text{int}} = -\sum_l U_l \sum_{\mathbf{k}, \mathbf{k}'} c_l^\dagger(\mathbf{k}') c_l^\dagger(-\mathbf{k}') c_l(-\mathbf{k}) c_l(\mathbf{k})$, which includes purely intraband pairing channels. Note that we can write the interaction in the orbital basis which is the starting point within the tight-binding approach, and then project to the band basis. However, this would cause complications, both in additional form factors and possible interband pairing interactions, which would partly disobey the decomposition that we used. The order parameter can be related to the Green function as:

$$\begin{aligned}
\Delta_{i,\mathbf{A}}(x, y) &= -\frac{1}{2} V(x-y) \text{Tr}[\tau_i G_{\mathbf{A}}(x, y)] \\
&= -\frac{1}{2} \int [dp] \int [dq] e^{-i(p+q)\cdot(x-y)} V(p) \text{Tr}[\tau_i G_{\mathbf{A}}(q)] \\
\Delta_{i,\mathbf{A}}(k) &= \int [dz] e^{ik\cdot z} \Delta_{i,\mathbf{A}}(z) \\
&= -\frac{1}{2} \int [dp] \int [dq] \int [dz] e^{i(k-p-q)\cdot z} V(p) \text{Tr}[\tau_i G_{\mathbf{A}}(q)] \\
&= -\frac{1}{2} \int [dp] \int [dq] (2\pi)^2 \delta(k-p-q) V(p) \text{Tr}[\tau_i G_{\mathbf{A}}(q)] \\
&= -\frac{1}{2} \int [dq] V(k-q) \text{Tr}[\tau_i G_{\mathbf{A}}(q)], \tag{K1}
\end{aligned}$$

where $i = x$ corresponds to the real part, and $i = y$ corresponds to the imaginary part. The vertex correction in a single band is accordingly given by:

$$\begin{aligned}
\Lambda_i^\mu(x, y, z) &= -\frac{\delta\Delta_{i,\mathbf{A}}(x, y)}{\delta A_\mu(z)} \\
&= \frac{1}{2} V(x-y) \text{Tr} \left[\tau_i \frac{\delta G_{\mathbf{A}}(x, y)}{\delta A_\mu(z)} \right] \\
&= -\frac{1}{2} V(x-y) \text{Tr} \left[\tau_i G_{\mathbf{A}}(x, y) \frac{\delta G_{\mathbf{A}}^{-1}(x, y)}{\delta A_\mu(z)} G_{\mathbf{A}}(x, y) \right] \\
\Lambda_i^\mu(k, \omega) &= -\int [dp] \frac{V(k-p)}{2} \text{Tr} [\tau_i G(p_0 + \omega, \mathbf{p}) \Gamma^\mu(p, \omega) G(p)] \tag{K2}
\end{aligned}$$

$$\Lambda_i^\mu(k, \omega) = -\int dp \frac{V(k-p)}{2} \text{Tr} \left[\tau_i G(p + \omega) \times \left(\gamma^\mu(p) + \sum_j \Lambda_j^\mu(p, \omega) \tau_j \right) G(p) \right], \tag{K3}$$

which can be converted to the multiband case by a substitution $\tau_i \rightarrow \tau_i \otimes E_l$ and $V(k-p) \rightarrow V_l(k-p)$, where $[E_l]_{ab} = \langle a | P_l | b \rangle$, with a, b being the orbital indices and l being the Bloch vector with a band index l in the normal

phase. We also note that $G^{-1}(k) = k_0 - H_{\text{BdG}}(\mathbf{k})$, which when assuming a decomposition $H_{\text{BdG}}(\mathbf{k}) = \sum_l M_l(\mathbf{k}) \otimes P_l(\mathbf{k})$, takes the form:

$$M_l(\mathbf{k}) = \begin{pmatrix} \epsilon_l(\mathbf{k}) & \Delta_l(\mathbf{k}) \\ \Delta_l^\dagger(\mathbf{k}) & -\epsilon_l(\mathbf{k}) \end{pmatrix} \quad (\text{K4})$$

$$\begin{aligned} G(k) &= \sum_l (k_0 I_2 - M_l)^{-1} \otimes P_l \\ &= - \sum_l \frac{1}{|\Delta_l|^2 + \epsilon_l^2 - k_0^2} \begin{pmatrix} k_0 + \epsilon_l & \Delta_l \\ \Delta_l^\dagger & k_0 - \epsilon_l \end{pmatrix} \otimes P_l. \end{aligned} \quad (\text{K5})$$

Importantly, this is only true if parity remains intact and we only have intraband interactions. A quick sanity check for the order parameter with $V(k - q) = g$, and for a single band, obtains:

$$\begin{aligned} \Delta &= g \int [d\mathbf{q}] \int_{-\infty}^{\infty} dq_0 \frac{\Delta}{|\Delta|^2 + \epsilon^2 - q_0^2} \\ &= \frac{g}{2} \int [d\mathbf{q}] \frac{\Delta}{\tilde{\epsilon}} [f(-\tilde{\epsilon}) - f(\tilde{\epsilon})] \\ &= \frac{g}{2} \int [d\mathbf{q}] \frac{\Delta}{\tilde{\epsilon}} \tanh \frac{\beta \tilde{\epsilon}}{2}. \end{aligned} \quad (\text{K6})$$

Furthermore, assuming that Δ_l has no \mathbf{k} -dependence, we simply have $V_l(k - p) = g_l$, and thus $\Lambda_i^\mu(k, i\Omega)$ drops the \mathbf{k} -dependence. We note that $\Lambda_{i,l}^\mu$ is nothing but an index, so can be extracted out of the trace. Then Eq. (K3) becomes:

$$\begin{aligned} \Lambda_{i,l}^\mu(\omega) &= -\frac{g_l}{2} \int [dp] \text{Tr} \left[\tau_i E_l G(p + \omega) \times \left(\gamma^\mu(p) + \sum_{j,l'} \Lambda_{j,l'}^\mu(\omega) \tau_j E_{l'} \right) G(p) \right] \\ \frac{2}{g_l} \Lambda_{i,l}^\mu(\omega) &= - \int [dp] \text{Tr} [\tau_i E_l G(p + \omega) \gamma^\mu(\mathbf{q}) G(p)] - \sum_{j,l'} \Lambda_{j,l'}^\mu \int [dp] \text{Tr} [\tau_i E_l G(p + \omega) \tau_j E_{l'} G(p)] \\ Q_{i,l}^\mu(\omega) &= \sum_{j,l'} \left(\frac{2}{g_l} \delta_{i,l;j,l'} - Q_{i,l;j,l'}(\omega) \right) \Lambda_{j,l'}^\mu(\omega), \end{aligned} \quad (\text{K7})$$

where we introduce terms that are defined as:

$$\begin{aligned} Q_{i,l}^\mu(\omega) &= - \int [dp] \text{Tr} [\tau_i E_l G(p + \omega) \gamma^\mu(\mathbf{q}) G(p)] \\ &= - \sum_{l'} \int [dp] \text{Tr} \left[G_{l'}(p) \tau_i G_l(p + \omega) \gamma_{l,l'}^\mu(\mathbf{q}) \right], \end{aligned} \quad (\text{K8})$$

$$\begin{aligned} Q_{x,l}^\mu(\omega) &= - \sum_{l'} \int [dp] \frac{\Delta_{l'}(p_0 + \omega + \epsilon_l) + \Delta_{l'}^*(p_0 + \epsilon_{l'}) + \Delta_l(p_0 - \epsilon_{l'}) + \Delta_l^*(p_0 + \omega - \epsilon_l)}{(|\Delta_{l'}|^2 + \epsilon_{l'}^2 - p_0^2)[|\Delta_l|^2 + \epsilon_l^2 - (p_0 + \omega)^2]} \text{Tr} \left[P_{l'}(\mathbf{q}) P_l(\mathbf{q}) h_{l,l'}^\mu(\mathbf{q}) \right] \\ &= -2 \sum_{l'} \int [d\mathbf{q}] \{ I_1(l, l') (\Delta_{x,l} + \Delta_{x,l'}) + I_0(l, l') [\omega \Delta_{x,l'} + i(\epsilon_l \Delta_{y,l'} - \epsilon_{l'} \Delta_{y,l})] \} h_{l,l'}^\mu(\mathbf{q}) \delta_{l,l'} \\ &= -2 \int [d\mathbf{q}] [2\Delta_{x,l} I_1(l, l) + \omega \Delta_{x,l} I_0(l, l)] h_{l,l}^\mu(\mathbf{q}), \end{aligned} \quad (\text{K9})$$

$$\begin{aligned} Q_{y,l}^\mu(\omega) &= -i \sum_{l'} \int [dp] \frac{\Delta_{l'}(p_0 + \omega + \epsilon_l) - \Delta_{l'}^*(p_0 + \epsilon_{l'}) + \Delta_l(p_0 - \epsilon_{l'}) - \Delta_l^*(p_0 + \omega - \epsilon_l)}{(|\Delta_{l'}|^2 + \epsilon_{l'}^2 - p_0^2)[|\Delta_l|^2 + \epsilon_l^2 - (p_0 + \omega)^2]} \text{Tr} \left[P_{l'}(\mathbf{q}) P_l(\mathbf{q}) h_{l,l'}^\mu(\mathbf{q}) \right] \\ &= 2 \sum_{l'} \int [d\mathbf{q}] \{ I_1(l, l') (\Delta_{y,l} + \Delta_{y,l'}) + I_0(l, l') [\omega \Delta_{y,l'} - i(\epsilon_l \Delta_{x,l'} - \epsilon_{l'} \Delta_{x,l})] \} h_{l,l'}^\mu(\mathbf{q}) \delta_{l,l'} \\ &= 2 \int [d\mathbf{q}] [2\Delta_{y,l} I_1(l, l) + \omega \Delta_{y,l} I_0(l, l)] h_{l,l}^\mu(\mathbf{q}), \end{aligned} \quad (\text{K10})$$

$$Q_{i,l;j,l'}(\omega) = - \int [dp] \text{Tr} [\tau_i E_l G(p + \omega) \tau_j E_{l'} G(p)]$$

$$\begin{aligned}
&= - \int [dp] \text{Tr}[\tau_i G_l(p + \omega) \tau_j G_{l'}(p)] \text{Tr}[P_l P_{l'}] \\
&= - \int [dp] \text{Tr}[\tau_i G_l(p + \omega) \tau_j G_l(p)] \delta_{l,l'} ,
\end{aligned} \tag{K11}$$

$$Q_{x,l;x,l}(\omega) = -2 \int [d\mathbf{q}] (\Delta_{x,l}^2 - \Delta_{y,l}^2 - \epsilon_l^2) I_0(l, l) + \omega I_1(l, l) + I_2(l, l) , \tag{K12}$$

$$Q_{y,l;y,l}(\omega) = -2 \int [d\mathbf{q}] (\Delta_{y,l}^2 - \Delta_{x,l}^2 - \epsilon_l^2) I_0(l, l) + \omega I_1(l, l) + I_2(l, l) , \tag{K13}$$

$$Q_{x,l;y,l}(\omega) = 4 \int [d\mathbf{q}] (2\Delta_{x,l} \Delta_{y,l} + i\epsilon_l \omega) I_0(l, l) , \tag{K14}$$

$$Q_{y,l;x,l}(\omega) = 4 \int [d\mathbf{q}] (2\Delta_{x,l} \Delta_{y,l} - i\epsilon_l \omega) I_0(l, l) , \tag{K15}$$

and where we implicitly used that $\gamma_{l,l'}^\mu = I_2 \otimes h_{l,l'}^\mu$.

Interestingly, in the band basis, all interband terms vanish when we only have an intraband interaction, and all terms contain no information of the quantum geometry of the band. Above, with $\tilde{\epsilon}_l > 0$ for clarity, we have defined I_i as:

$$\begin{aligned}
I_0(l, l') &= \int dp_0 \frac{1}{(\tilde{\epsilon}_{l'}^2 - p_0^2)[\tilde{\epsilon}_l^2 - (p_0 + \omega)^2]} \\
&= \frac{1}{\beta} \sum_z \frac{1}{(\tilde{\epsilon}_{l'}^2 - z^2)[\tilde{\epsilon}_l^2 - (z + i\omega)^2]} \\
&= \sum_{z=\pm\tilde{\epsilon}_{l'}, \pm\tilde{\epsilon}_l - i\omega} f(z) R_0(z) \\
&\rightarrow R_0(-\tilde{\epsilon}_{l'}) + R_0(-\tilde{\epsilon}_l - \omega) \\
&= \frac{\tilde{\epsilon}_l + \tilde{\epsilon}_{l'}}{2\tilde{\epsilon}_l \tilde{\epsilon}_{l'} [(\tilde{\epsilon}_{l'} + \tilde{\epsilon}_l)^2 - \omega^2]} ,
\end{aligned} \tag{K16}$$

$$\begin{aligned}
I_1(l, l') &= \int dp_0 \frac{p_0}{(\tilde{\epsilon}_{l'}^2 - p_0^2)[\tilde{\epsilon}_l^2 - (p_0 + \omega)^2]} \\
&= \frac{1}{\beta} \sum_z \frac{iz}{(\tilde{\epsilon}_{l'}^2 + z^2)[\tilde{\epsilon}_l^2 - (z + i\omega)^2]} \\
&= \sum_{z=\pm\tilde{\epsilon}_{l'}, \pm\tilde{\epsilon}_l - \omega} f(z) R_1(z) \\
&\rightarrow R_1(-\tilde{\epsilon}_{l'}) + R_1(-\tilde{\epsilon}_l - \omega) \\
&= -\frac{\omega}{2\tilde{\epsilon}_l [(\tilde{\epsilon}_{l'} + \tilde{\epsilon}_l)^2 - \omega^2]} ,
\end{aligned} \tag{K17}$$

$$\begin{aligned}
I_2(l, l') &= \int dp_0 \frac{p_0^2}{(\tilde{\epsilon}_{l'}^2 - p_0^2)[\tilde{\epsilon}_l^2 - (p_0 + \omega)^2]} \\
&= \frac{1}{\beta} \sum_z \frac{z^2}{(\tilde{\epsilon}_{l'}^2 - z^2)[\tilde{\epsilon}_l^2 - (z + i\omega)^2]} \\
&= \sum_{z=\pm\tilde{\epsilon}_{l'}, \pm\tilde{\epsilon}_l - \omega} f(z) R_2(z) \\
&\rightarrow R_2(-\tilde{\epsilon}_{l'}) + R_2(-\tilde{\epsilon}_l - \omega) \\
&= \frac{\omega^2 - \tilde{\epsilon}_l(\tilde{\epsilon}_l + \tilde{\epsilon}_{l'})}{2\tilde{\epsilon}_l [(\tilde{\epsilon}_{l'} + \tilde{\epsilon}_l)^2 - \omega^2]} ,
\end{aligned} \tag{K18}$$

where R_i denote the residue of the integrand of I_i , and ω_n are the odd Matsubara frequencies. We also take the zero temperature limit to obtain simple analytic form. Since ω is due to incoming photon, it has to be an element of the even Matsubara frequencies, thus the corresponding poles in the imaginary axis remain unshifted. With only the $l = l'$ integral being relevant, we list down the zero temperature results below:

$$I_0(l, l) = \frac{1}{\tilde{\epsilon}_l(4\tilde{\epsilon}_l^2 - \omega^2)} , \tag{K19}$$

$$I_1(l, l) = \frac{\omega}{2\tilde{\epsilon}_l(4\tilde{\epsilon}_l^2 - \omega^2)}, \quad (\text{K20})$$

$$I_2(l, l) = \frac{\omega^2 - 2\tilde{\epsilon}_l^2}{2\tilde{\epsilon}_l(4\tilde{\epsilon}_l^2 - \omega^2)}. \quad (\text{K21})$$

As such, the correlation function can be simplified as:

$$Q_{x,l}^\mu(\omega) = -4 \int [d\mathbf{q}] \frac{\omega \Delta_{x,l}}{\tilde{\epsilon}_l(4\tilde{\epsilon}_l^2 - \omega^2)} \partial^\mu \epsilon_l, \quad (\text{K22})$$

$$Q_{y,l}^\mu(\omega) = 4 \int [d\mathbf{q}] \frac{\omega \Delta_{y,l}}{\tilde{\epsilon}_l(4\tilde{\epsilon}_l^2 - \omega^2)} \partial^\mu \epsilon_l, \quad (\text{K23})$$

$$\begin{aligned} Q_{x,l;x,l} &= -2 \int [d\mathbf{q}] \frac{2(\Delta_{x,l}^2 - \Delta_{y,l}^2 - \epsilon_l^2) + \omega^2 + \omega^2 - 2\tilde{\epsilon}_l^2}{2\tilde{\epsilon}_l(4\tilde{\epsilon}_l^2 - \omega^2)} \\ &= -2 \int [d\mathbf{q}] \frac{2\Delta_l^2 \cos^2 \phi - 2\tilde{\epsilon}_l^2 + \omega^2}{\tilde{\epsilon}_l(4\tilde{\epsilon}_l^2 - \omega^2)}, \end{aligned} \quad (\text{K24})$$

$$\begin{aligned} Q_{y,l;y,l} &= -2 \int [d\mathbf{q}] \frac{2(\Delta_{y,l}^2 - \Delta_{x,l}^2 - \epsilon_l^2) + \omega^2 + \omega^2 - 2\tilde{\epsilon}_l^2}{2\tilde{\epsilon}_l(4\tilde{\epsilon}_l^2 - \omega^2)} \\ &= -2 \int [d\mathbf{q}] \frac{2\Delta_l^2 \sin^2 \phi - 2\tilde{\epsilon}_l^2 + \omega^2}{\tilde{\epsilon}_l(4\tilde{\epsilon}_l^2 - \omega^2)}, \end{aligned} \quad (\text{K25})$$

$$Q_{x,l;y,l}(\omega) = 4 \int [d\mathbf{q}] \frac{2\Delta_{x,l}\Delta_{y,l} + i\epsilon_l\omega}{\tilde{\epsilon}_l(4\tilde{\epsilon}_l^2 - \omega^2)}, \quad (\text{K26})$$

$$Q_{y,l;x,l}(\omega) = 4 \int [d\mathbf{q}] \frac{2\Delta_{x,l}\Delta_{y,l} - i\epsilon_l\omega}{\tilde{\epsilon}_l(4\tilde{\epsilon}_l^2 - \omega^2)}. \quad (\text{K27})$$

$$(\text{K28})$$

We note that with only the intraband interaction, no information of the quantum geometry is included within the vertex correction. Finally, we note that the vertex correction can be obtained by solving the set of linear equations that read:

$$Q_{x,l}^\mu(\omega) = \left(\frac{2}{g_l} - Q_{x,l;x,l}(\omega) \right) \Lambda_{x,l}^\mu(\omega) - Q_{x,l;y,l}(\omega) \Lambda_{y,l}^\mu(\omega), \quad (\text{K29})$$

$$Q_{y,l}^\mu(\omega) = \left(\frac{2}{g_l} - Q_{y,l;y,l}(\omega) \right) \Lambda_{y,l}^\mu(\omega) - Q_{y,l;x,l}(\omega) \Lambda_{x,l}^\mu(\omega). \quad (\text{K30})$$

Vertex correction only affects the transitions of form $(l, \pm) \rightarrow (l, \pm)$ and $(l, \pm) \rightarrow (l, \mp)$. The former correspond to the intraband response, while the latter intersector transitions are forbidden, given that $H_{l,\pm;l,\mp}^\mu = 0$.

We conclude by stressing that there is a fundamental difference between working in the band basis and in the orbital basis. In the orbital basis, even limited to the scope of an onsite interaction only, as soon as we convert to the band basis, a general interaction would be both interband and intraband. This dissimilitude could explain why in Ref. [65] a significant difference due to the band mixing can arise, whereas in our case, there is no effect beyond the intraband pairing in the linear optical response of the superconducting state. However, this subtle distinction does have an interesting consequence in the third-order response; namely, a new type of transition is now possible, which is because we can have a multiple vertex correction.

Appendix L: Additional numerical results

In the following, we present further numerical results for the photoconductivities of Euler superconductors realized in the Lieb and kagome lattice models (see Fig. 8 and Fig. 9, correspondingly), which were not included in the main text, but for completeness are provided below.

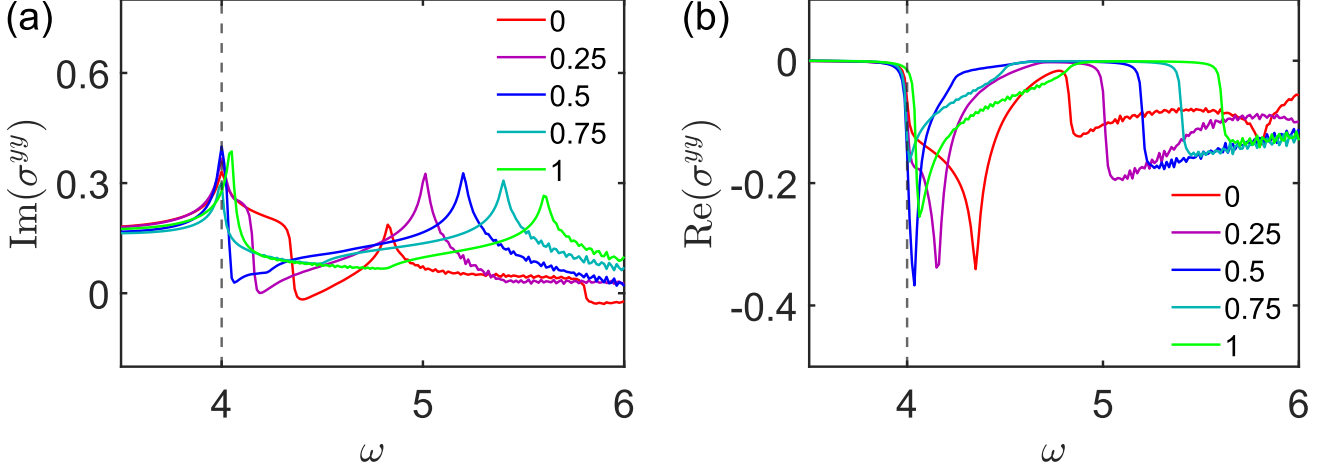


FIG. 8. Real and imaginary part of photoconductivity σ^{yy} , with the same parametrization as in Fig. 3. We note that the change in conductivity profile is highly non-trivial when the Euler node is gapped. For example, σ^{yy} can be compared with σ^{xx} in Fig. 3, accordingly.

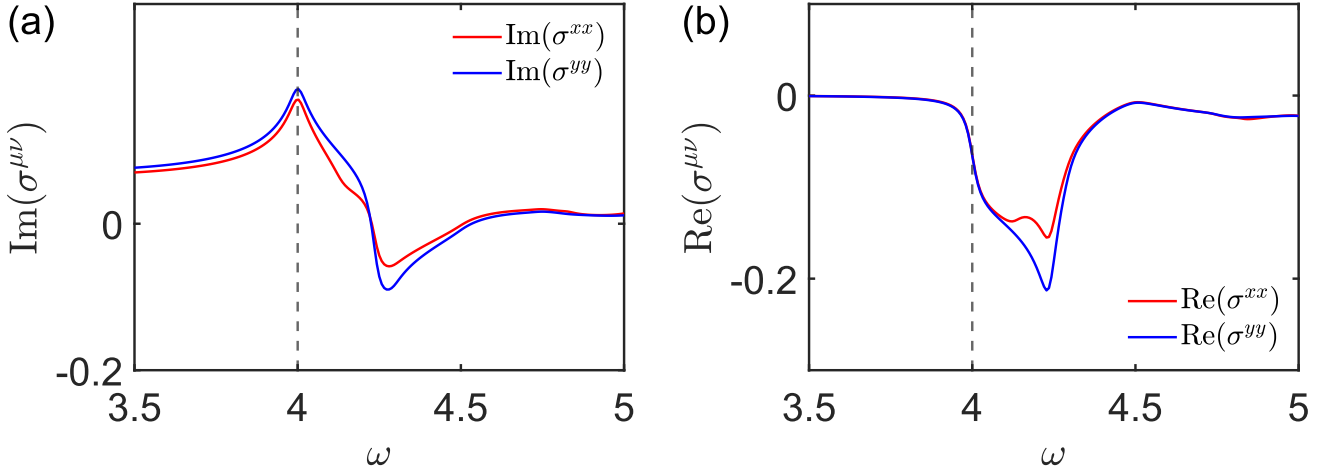


FIG. 9. Real and imaginary part of photoconductivities σ^{xx} and σ^{yy} , for the superconducting phase realized in a kagome lattice model with $\chi = 1$ [32, 45]. We adapt only the nearest neighbour hopping, and set all onsite potentials to zero, consistently with the model parametrization of Refs. [32, 45]. We note that similarly to the Lieb lattice model, a node of patch Euler class $\chi = 1$ is between the flat and quadratic bands. We set the chemical potential to coincide with the node, similarly as in Fig. 3. We observe an analogous quantized jump in the real part of linear conductivity in the kagome lattice model.